Li et al. *Zool. Res.* 2023, 44(3): 636−649
https://doi.org/10.24272/j.issn.2095-8137.2022.531

ZR | Zoological Research

Article Open Access

EPAS1 prevents telomeric damage-induced senescence by enhancing transcription of *TRF1*, *TRF2*, and *RAD50*

Kai-Qin Li[1,#], Gao-Jing Liu[1,#], Xiu-Yun Liu[1,3,#], Qiong-Fang Chen[1,#], Xiao-Yan Huang[1,3,#], Qiu Tu[1], Jiao Zhang[1], Qing Chang[1,4], Yun-Hua Xie[1,4], Rong Hua[1,2], Dong-Ming Xu[1,2], Zhen Liu[1,2], Bo Zhao[1,4,*]

[1] *Key Laboratory of Animal Models and Human Disease Mechanisms of the Chinese Academy of Sciences & Yunnan Province, KIZ-CUHK Joint Laboratory of Bioresources and Molecular Research in Common Diseases, Kunming Institute of Zoology, Chinese Academy of Sciences, Kunming, Yunnan* 650201, *China*

[2] *State Key Laboratory of Genetic Resources and Evolution, Kunming Institute of Zoology, Chinese Academy of Sciences, Kunming, Yunnan* 650201, *China*

[3] *University of Chinese Academy of Sciences, Beijing* 100049, *China*

[4] *Primate Facility, National Research Facility for Phenotypic & Genetic Analysis of Model Animals, and National Resource Center for Non-Human Primates, Kunming Institute of Zoology, Chinese Academy of Sciences, Kunming, Yunnan* 650201, *China*

ABSTRACT

Telomeres are nucleoprotein structures located at the end of each chromosome, which function in terminal protection and genomic stability. Telomeric damage is closely related to replicative senescence *in vitro* and physical aging *in vivo*. As relatively long-lived mammals based on body size, bats display unique telomeric patterns, including the up-regulation of genes involved in alternative lengthening of telomeres (ALT), DNA repair, and DNA replication. At present, however, the relevant molecular mechanisms remain unclear. In this study, we performed cross-species comparison and identified *EPAS1*, a well-defined oxygen response gene, as a key telomeric protector in bat fibroblasts. Bat fibroblasts showed high expression of EPAS1, which enhanced the transcription of shelterin components TRF1 and TRF2, as well as DNA repair factor RAD50, conferring bat fibroblasts with resistance to senescence during long-term consecutive expansion. Based on a human single-cell transcriptome atlas, we found that *EPAS1* was predominantly expressed in the human pulmonary endothelial cell subpopulation. Using *in vitro*-cultured human pulmonary endothelial cells, we confirmed the functional and mechanistic conservation of EPAS1 in telomeric protection between bats and humans. In addition, the EPAS1 agonist M1001 was shown to be a protective compound against bleomycin-induced pulmonary telomeric damage and senescence. In conclusion, we identified a potential mechanism for regulating telomere stability in human pulmonary diseases associated with aging, drawing insights from the longevity of bats.

Keywords: Bat; Telomere; Senescence; EPAS1; M1001; Pulmonary endothelial cell

INTRODUCTION

Telomeres are cap-like structures found at the end of linear chromosomes. Telomeres are composed of repetitive nucleotide sequences, associated proteins, and RNA components (De Lange, 2005). The shelterin complex, composed of TRF1, TRF2, POT1, RAP1, TIN2, and TPP1, is vital for telomeric stability in mammalian cells. TRF1 and TRF2 are homodimers that bind to telomeric double-stranded DNA (Bilaud et al., 1997; Broccoli et al., 1997; Van Steensel & De Lange, 1997). POT1 and TPP1 form a heterodimer that binds to the telomeric 3' tail (Lei et al., 2004; Loayza & De Lange, 2003). TIN2 is a linker that connects TRF1 and TRF2 dimers with POT1-TPP1 to form the shelterin complex (O'Connor et al., 2006). RAP1 interacts with TRF2 as an accessory to protect telomeres, especially critically short telomeres (Rai et al., 2016; Sfeir et al., 2010). In addition to protecting chromosome ends, the shelterin complex is also responsible for telomeric length sensing and telomerase activity regulation (Lim & Cech, 2021). In addition, the CST complex, composed of CTC1, STN1, and TEN1, and DNA damage response (DDR) proteins collaborate with shelterin to

Received: 23 February 2023; Accepted: 11 April 2023; Online: 17 April 2023

Foundation items: This work was supported by the Applied Basic Research Programs of Science and Technology Commission Foundation of Yunnan Province (202201AS070044), National Key Research & Developmental Program of China (2021YFA0805701), Chinese Academy of Sciences (CAS) "Light of West China" Program (xbzg-zdsys-202113), and Kunming Science and Technology Bureau (2022SCP007)

[#]Authors contributed equally to this work

*Corresponding author, E-mail: zhaobo@mail.kiz.ac.cn

maintain telomeric length and stability. CST competes with TPP1-POT1 to bind to the telomeric 3' tail and sequesters telomerase from telomeric tail engagement (Chen et al., 2012). CST is required for the timely termination of the telomere extension process, as well as for the recruitment of DNA polymerase α-primase (pol α-primase) to the nascent telomeric tail for C-strand fill-in (Casteel et al., 2009). DDR proteins, such as Ku70 and MRN (MRE11-RAD50-NBS1), protect single-stranded and double-stranded telomeric DNA from degeneration (Celli et al., 2006; Limbo et al., 2018; Ribes-Zamora et al., 2013). Additionally, long non-coding telomeric repeat-containing RNA (TERRA) is enriched in telomeres to protect chromosome ends from telomere loss (Azzalin et al., 2007). Overall, telomere maintenance is a complex process regulated by large-scale chromatin architectural modulations and dynamic molecular interactions (Lim & Cech, 2021). Disruption of the shelterin complex leads to telomere dysfunction-induced foci (TIF), chromosome fusion, and mitotic defects. Cells with telomeric damage are sensitized to apoptosis or senescence in different contexts (Martínez & Blasco, 2010).

As the core subunits of the shelterin complex, the expression and function of TRF1 and TRF2 are precisely controlled. For instance, *TRF1* and *TRF2* are transcriptionally co-promoted by the BRM-SWI/SNF complex (Wu et al., 2020). Transcription factors Sp1 and β-catenin promote TRF2 transcription (Diala et al., 2013; Dong et al., 2009), while miR-23a and miR155 inhibit TRF2 and TRF1 translation by directly targeting their 3'-untranslated regions (3'-UTR), respectively (Dinami et al., 2014; Luo et al., 2015). In addition, post-translational modifications, e.g., phosphorylation, ubiquitylation, SUMOylation, and PARylation, play critical roles in the functions of TRF1 and TRF2 (Walker & Zhu, 2012). The binding of TRF1 to telomeric DNA relies on the phosphorylation at Thy22 by CK2 kinase. Inhibition of CK2 impairs TRF1 loading onto telomeres and its stability (Kim et al., 2008). TRF2 is degraded by the p53-induced E3 ligase Siah1 in the process of replicative senescence in human fibroblasts (Fujita et al., 2010). Indeed, deletion of TRF1 promotes the accumulation of fragile telomeres and telomeric fusions (Sfeir et al., 2009). Removal of TRF2 from telomeres by the overexpression of a dominant-negative allele of TRF2 that lacks the basic and Myb-like domains or by the deletion of TRF2 altogether results in the loss of telomere overhang and end-to-end fusions (Van Steensel et al., 1998). Despite these advances in our understanding of the assembly and interactions of telomeric components, a clear map of the regulatory pathways that control the expression of TRF1 and TRF2, as well as other telomeric subunits, remains elusive.

Bats exhibit extreme longevity given their body size. Many bat species show limited senescence (Fleischer et al., 2017; Wilkinson & Adams, 2019) and few signs of aging (Power et al., 2021). Regarding telomeres, bat species show unique patterns regarding telomere length and telomerase expression. In a large-scale comparative study of over 60 mammalian cell lines, including four bat species (i.e., flying fox, Mexican free-tail bat, big-brown bat, and little-brown bat), the flying fox displayed short telomeres (9 kb), while the other three species contained long telomeres (26–30 kb) (Gomes et al., 2011). Significant telomere shortening with age has been reported in certain bat species, such as the greater horseshoe bat (*Rhinolophus ferrumequinum*) and common bent-wing bat (*Miniopterus schreibersii*), but not in the longest-lived genus *Myotis* (Foley et al., 2018). Despite the absence of telomerase expression in *Myotis* wing fibroblasts and blood transcriptomes, their telomeres appear to be protected from age-related attrition. Notably, up-regulated genes involved in alternative lengthening of telomeres (ALT) (Cesare & Reddel, 2010; Mendez-Bermudez et al., 2012), DNA repair, and DNA replication are enriched in *Myotis* transcriptomes, suggesting the utilization of ALT mechanisms to protect telomeres and an enhanced ability to cope with DNA damage (Foley et al., 2018). Indeed, compared to human and mouse fibroblasts, bat (*Pteropus alecto* and *Myotis davidii*) fibroblasts exhibit elevated expression of the ATP-binding cassette (ABC) transporter ABCB1 to enhance efflux of genotoxic compounds from cells and ensure genomic stability (Koh et al., 2019). Thus, these studies highlight the potential of bats as excellent models for investigating telomeres and genomic stability. However, a comprehensive understanding of the underlying molecular mechanisms is required to further explore bat-specific properties.

In the current study, we explored the potentially distinct molecular mechanisms underlying telomeric stabilization in bats and evaluated the feasibility of translating this mechanism into clinical application for anti-aging in humans. We first established a comparative cellular system composed of primary fibroblasts from Chinese horseshoe bats (*Rhinolophus sinicus*), Rickett's big-footed bats (*Myotis ricketti*), rhesus macaques (*Macaca mulatta*), humans (*Homo sapiens*), Wistar rats (*Rattus norvegicus*), and C57BL/6 mice (*Mus musculus*). We detected unique telomeric patterns in the bat fibroblasts, manifesting as giant and heterogeneous telomere foci when performing telomere fluorescence *in-situ* hybridization (T-FISH). The bat fibroblasts maintained low levels of TIF and were resistant to replicative senescence in consecutive expansion. Regarding the potential underlying mechanism, we identified EPAS1 as a key regulator, which transcriptionally promoted the expression levels of *TRF1*, *TRF2*, and *RAD50*. We also confirmed the functional and mechanistic conservation of EPAS1 in human pulmonary endothelial cells. The EPAS1 agonist M1001 (Wu et al., 2019) enhanced telomeric stability and delayed senescence in the context of bleomycin (BLM)-induced pulmonary damage.

MATERIALS AND METHODS

Cells and culture conditions

Wistar rat, rhesus macaque, human, and NIH3T3 primary fibroblasts were purchased from the Conservation Genetics CAS Kunming Cell Bank (China). Primary fibroblasts from mice were isolated from C57BL/6 mouse embryos on embryonic day 13.5 (E13.5). Primary fibroblasts from Chinese horseshoe bat and Rickett's big-footed bat were kindly provided by the Peng Shi Lab at the Kunming Institute of Zoology, CAS. Fibroblasts of bats, humans, rats, and monkeys were primarily isolated from adult ear skin tissues. The human lung fibroblast α (HLF-α) cell line was purchased from the BLUEFBIO company (Shanghai, China). All cells were cultured in Dulbecco's Modified Eagle Medium (DMEM) (Gibco, USA, Cat. No. 11965) supplemented with 10% fetal bovine serum (FBS) (Gibco, USA, Cat. No. 10099141C) under 37 °C and 5% CO_2 conditions for three days in each passage. Cells were expanded based on 0.05% trypsin/ethylenediaminetetraacetic acid (EDTA) digestion. All cells were authenticated at the Conservation Genetics CAS

Kunming Cell Bank using short tandem repeat DNA profiling. Regular mycoplasma testing was performed using a LookOut Mycoplasma PCR Detection Kit (Sigma-Aldrich, USA, Cat. No. MP0035).

Reagents and antibodies

Bromodeoxyuridine (BrdU) was purchased from Sigma-Aldrich (USA, Cat. No. B5002). PT2385 was purchased from Selleck Chem (USA, Cat. No. S8352). M1001 was purchased from Selleck Chem (USA, Cat. No. S1232). TRIzol reagent was purchased from Tiangen (Germany, Cat. No. DP424). Lipofectamine 2000 was purchased from Thermo Fisher (USA, Cat. No. 11668500). 4',6'-Diamidino-2-phenylindole (DAPI) was purchased from Sigma-Aldrich (USA, Cat. No. D9542). Hydrogen peroxide (H_2O_2) was purchased from Tianjin Chemical Industry (China). The (T_2AG_3)-Cy3-labeled peptide nucleic acid telomeric probe was purchased from PANAGENE (Korea, Cat. No. F1006). BLM was purchased from Selleck Chem (USA, Cat. No. S1214). Collagenase was purchased from Sigma-Aldrich (USA, Cat. No. C5138). Hyaluronidase was purchased from Sigma-Aldrich (USA, Cat. No. H3884). DNase1 was purchased from Sigma-Aldrich (USA, Cat. No. D5025). The Reactive Oxygen Species Assay Kit was purchased from Beyotime (China, Cat. No. S0033M).

Homology analysis of amino acid sequences was performed using MEGA (v7.0) and GeneDoc (v2.7.0), with the results shown in Supplementary Table S1. The following antibodies were obtained: rabbit anti-smooth muscle actin (α-SMA, Proteintech, USA, Cat. No. 14395-1-AP, 1:500 for immunofluorescence), mouse anti-CDKN2A/p16INK4a (Santa Cruz, USA, Cat. No. sc-1661, 1:1 000 for immunoblotting), mouse anti-p21 Waf1/Cip1/CDKN1A (Santa Cruz, USA, Cat. No. sc-6246, 1:1 000 for immunoblotting), mouse anti-cyclin A (Santa Cruz, USA, Cat. No. sc-239, 1:1 000 for immunoblotting), rabbit anti-PPP1CC (Proteintech, USA, Cat. No. 11082-1-AP, 1:1 000 for immunoblotting), mouse anti-PPP1CA (Proteintech, USA, Cat. No. 67070-1-Ig, 1:1 000 for immunoblotting), rabbit anti-CD34 (Proteintech, USA, Cat. No. 14486-1-AP, 1:500 for immunofluorescence), rat anti-BrdU (Novus, USA, Cat. No. NB500-169, 1:500 for immunofluorescence), rabbit anti-γH2A.X (Cell Signaling Technology, USA, Cat. No. 9719S, 1:1 000 for immunoblotting and 1:500 for immunofluorescence), mouse anti-γH2A.X (Merck, Germany, Cat. No. 05-636, 1:500 for immunofluorescence), rabbit anti-EPAS1 (Novus, USA, Cat. No. NB100-122, 1:1 000 for immunoblotting and 1:500 for immunofluorescence), rabbit anti-c-Fos (BioLegend, USA, Cat. No. 641401, 1:1 000 for immunoblotting), rabbit anti-TRF1 (Abcam, UK, Cat. No. ab129177, 1:1 000 for immunoblotting), rabbit anti-TRF2 (Cell Signaling Technology, USA, Cat. No. 13136, 1:1 000 for immunoblotting), rabbit anti-RAD50 (Abcam, UK, Cat. No. ab124682, 1:1 000 for immunoblotting), mouse anti-HNRNPK (Abcam, UK, Cat. No. ab39975, 1:1 000 for immunoblotting), mouse anti-β-actin (Sigma-Aldrich, USA, Cat. No. A2228, 1:1 000 for immunoblotting), and rabbit anti-ARNT (Proteintech, USA, Cat. No. 14105-1-AP, 1:1 000 for immunoblotting). Secondary antibodies for immunofluorescence were raised against rats (conjugated with Cyanine3, Thermo Fisher, USA, Cat. No. A-10522), rabbits (conjugated with Alexa 488, Thermo Fisher, USA, Cat. No. A-10680), or mice (conjugated with Alexa 488, Thermo Fisher, USA, Cat. No. A11029; conjugated with Alexa 555, Thermo Fisher, USA, Cat. No. A31570). Secondary antibodies used for immunoblotting were raised against rabbits (conjugated with horseradish peroxidase (HRP), Beyotime, China, Cat. No. A0208) or mice (conjugated with HRP, Beyotime, China, Cat. No. A0216).

Detection of intracellular reactive oxygen species (ROS)

Oxidation-sensitive fluorescent probe 2,7-dichlorofluorescein diacetate (DCFH-DA, Beyotime, China) was used to detect intracellular ROS levels. The DCFH-DA probe was diluted with DMEM to a final concentration of 10 μmol/L and added to cells for 20 min at 37 ºC. After that, 2,7-dichlorofluorescein (DCF) fluorescence was detected by flow cytometry (Becton, Dickinson, and Company, USA) at 488 nm (excitation wavelength) and 525 nm (emission wavelength). Approximately 20 000 cells were analyzed for each sample.

Measurement of 8-hydroxy-2 deoxyguanosine (8-OHdG)

The concentration of 8-OHdG was detected using a commercial enzyme-linked immunosorbent assay (ELISA) kit (Cloud-Clone CORP, Wuhan, China; Cat. No. CEA660Ge) according to the manufacturer's instructions. Briefly, gradient dilution standard or cell culture medium was added to 96-well plates coated with 8-OHdG monoclonal antibodies. Biotin-labeled antigens were added and incubated for 1 h at 37 °C. After washing three times, HRP solution was added to each well and incubated for 30 min at 37 °C. The addition of 3,3',5,5'-tetramethylbenzidine (TMB) to the plate and reaction with HRP for 15 min yields a blue-colored product. Termination of the reaction with acid changes the color to yellow. The depth of color is negatively correlated with 8-OHdG content in the sample. Absorbance at 450 nm was detected to reflect the 8-OHdG level.

BrdU incorporation assay

Normal cultured cells were incubated with 10 μmol/L BrdU for 60 min. After fixing with 4% paraformaldehyde (PFA) and permeabilizing with 0.2% Triton X-100/phosphate-buffered saline (PBS) (*V/V*) for 10 min, cells were treated with 2 mol/L HCl for 30 min. After that, cells were incubated with rat anti-BrdU primary antibody overnight at 4 °C, followed by goat anti-rat cyanine3 conjugated secondary antibody for 60 min. Slides were mounted with Permount (Polysciences, USA, Cat. No. 18606-20) and an Olympus scanning confocal microscope (FV1000, Japan) was used to capture the images.

Senescence-associated β-galactosidase (SA-β-gal) staining

SA-β-gal staining was performed using a SA-β-gal staining kit (Beyotime, China, Cat. No. C0602) according to the manufacturer's instructions. For cultured cells, cells were fixed with β-galactosidase staining fixative for 15 min, followed by washing with PBS three times. After washing, cells were incubated with staining solution overnight at 37 °C, washed with PBS three times, and examined using an inverted fluorescence microscope (ECLIPSE Ti, Japan).

Immunoblotting

Cells were lysed in radioimmunoprecipitation assay (RIPA) buffer (Thermo Fisher, USA, Cat. No. 89900) and heated to 95 °C for 10 min. Protein concentrations were determined using a protein assay dye (Bio-Rad, USA, Cat. No. #5000006) and Nanodrop spectrophotometer (USA). An equal amount of total protein was resolved using sodium dodecyl sulfate-polyacrylamide gel electrophoresis (SDS-PAGE) and transferred onto polyvinylidene difluoride (PVDF) membranes at 110 V for 2 h at 4 °C. Membranes were blocked with 5% bovine serum albumin (BSA) in Tris-HCl buffer solution (TBS) (*W/V*) containing 0.1% Tween 20 (TBS-T) for 1 h at room

temperature. Membranes were incubated overnight at 4 °C in primary antibodies and 4% BSA/TBS+0.025% sodium azide. Membranes were washed four times in TBS-T for 5 min at room temperature, incubated with HRP-conjugated secondary antibodies for 1 h at room temperature, then again washed four times in TBS-T at room temperature. The proteins were visualized using a chemiluminescence image analysis system (Tanon 5200, China) after incubation with the SuperSignal West Pico PLUS Chemiluminescent Substrate (Thermo Fisher, USA, Cat. No. 34580).

Telomere-γH2A.X immunofluorescence *in-situ* hybridization

Cultured cells were fixed with 4% PFA for 10 min, washed with PBS, and dehydrated in successive 70%, 85%, and 100% ethanol treatments (5 min each). Hybridization buffer (20 mmol/L Na_2HPO_4; 20 mmol/L Tris; 60% formamide; 2×saline sodium citrate (SSC, 0.3 mol/L NaCl, 30 mmol/L Na citrate, pH=7.4)) containing 0.05 pmol/L (T_2AG_3)-Cy3-labeled peptide nucleic acid (PNA) telomeric probe was added to the cells, followed by heating to 85 °C for 2 min. Cells were placed into a dark humidified chamber at 37 °C overnight. After 4% PFA fixation, the cells were re-stained with anti-γH2A.X or anti-EPAS1 antibodies following standard immunocytofluorescence protocols. DAPI staining was performed to label the nuclei. Slides were analyzed using an Olympus scanning confocal microscope (FV1000, Japan). For TIF analysis, three independent experiments (*n*=100 cells each) were performed by counting the co-localization of telomeric foci and γH2A.X. For telomere FISH-based quantification of telomere length, 20 cells were examined by measuring the integrated density of telomeric foci using ImageJ software (v1.8.0).

Luciferase reporter assay

The promoter regions of *TRF1*, *TRF2*, *RAD50*, and *VEGF* (1 000 bp upstream from the transcription start site (TSS)) in Supplementary Table S2 were synthesized (Tsingke Biotechnology, China) and constructed into the pGL4.11 vector (Promega, USA, Cat. No. E6661). The pGL4.11 constructs (150 ng) and internal control vector pRL-TK (30 ng, Promega, USA, Cat. No. E2241) were co-transfected into mouse fibroblasts using Lipofectamine 2000 (Thermo Fisher, USA). At 48 h post transfection, luminescence was measured using a Dual-Luciferase Reporter Assay System (Promega, USA, Cat. No. E1960) and Luminoskan Ascent instrument (Thermo Fisher, USA).

Quantitative reverse transcription polymerase chain reaction (qRT-PCR)

Total RNA was isolated using TRIzol reagent according to the manufacturer's instructions. Extracted RNA was used for qRT-PCR with a Reverse Transcription Kit (Takara, Japan, Cat. No. RR047A). qRT-PCR was performed using a TB Green™ Premix Ex Taq™ II Kit (Takara, Japan, Cat. No. RR820A) with the Bio-Rad Real-Time PCR platform (CFX-Connect™, USA). Primer sequences used for qRT-PCR are provided in Supplementary Table S3. The qRT-PCR-based quantification of telomere length was performed as described previously (Cawthon, 2002; Ropio et al., 2020).

Senescence-associated secretory phenotype (SASP) expression analysis

Adherent cells were washed three times with PBS and cultured with serum-free medium for 48 h. The serum-free medium was then collected and filtered using a 0.2 μm filter membrane. A Human Cytokine Array C1 Kit (RayBiotech, USA, Cat. No. AAH-INF-3-2) was used to detect SASP expression according to the manufacturer's guidelines. Briefly, membranes were incubated with blocking buffer and incubated with serum-free medium overnight at 4 °C. After washing with washing buffer, the membranes were incubated with biotinylated antibodies for 2 h at room temperature, then washed and incubated with streptavidin-HRP for 2 h at room temperature. After washing with washing buffer, the membranes were subjected to the chemiluminescence image analysis system (Tanon 5200, China) to visualize SASP expression signals.

Constructs and lentiviral infection

The short hairpin RNA (shRNA) sequences are provided in Supplementary Table S4. The shRNAs were constructed into pLKO.1 vectors through the enzymatic sites Age I/EcoR I. Both pLKO.1-shRNA and the pLVX system were used for lentiviral packaging. HEK293T cells were transfected using Lipofectamine 2000 (Thermo Fisher, USA). The lentivirus was harvested and filtered with a 0.45 μm filter 48 h post transfection. Cells infected with lentiviruses were selected in 0.5 μg/mL puromycin 48 h post infection.

RNA sequencing (RNA-seq) and bioinformatics analysis

Total RNA was isolated from the fibroblasts of bats (Chinese horseshoe bats) and laboratory mice using TRIzol reagent following the manufacturer's protocols. After validation of RNA quality and integrity, RNA libraries were created using a NEBNext Ultra RNA Library Prep Kit (Illumina, USA). Libraries were sequenced as paired-end 150 bp reads using the Illumina PE150 platform. Clean data were obtained by removing adapter sequences, low-quality reads, and low-quality bases using Trimmomatic v0.36 with default parameters. Gene expression levels were estimated using RSEM (v1.3.3)and DESeq2 (v1.34.0) to identify differentially expressed genes (DEGs) among one-to-one orthologous protein-coding genes between mice and bats (|fold-change|>2, *P*adj<0.05). The DEGs were used for Kyoto Encyclopedia of Genes and Genomes (KEGG) and Gene Ontology (GO) enrichment analyses with KOBAS-i.

Single-cell RNA-seq (scRNA-seq) data processing

A single-cell transcriptome atlas of the human lung was downloaded from the CZ CELLxGENE database (https://cellxgene.cziscience.com/collections/2f75d249-1bec-459b-bf2b-b86221097ced). We excluded data with lung diseases or COVID-19 infection. Only data collected from healthy lungs were used. Seurat (v4.1.1) was used for further data analysis and visualization. Different gene expression levels between various age groups were evaluated using the Mann-Whitney *U* test (two-tailed). Expression correlation between *EPAS1* and *TRF1*/*TRF2* in the single-cell transcriptome database of human pulmonary endothelial cells was calculated using Pearson correlation coefficients with Python (v3.9.16).

Animal assays and ethics statement

All animal procedures performed in this research were conducted in accordance with the guidelines approved by the Ethics Committee of the Kunming Institute of Zoology (approval number: IACUC-RE-202201004).

For the subcutaneous murine xenograft formation assay, six-week-old nude mice$^{Nu/Nu}$ were purchased from Charles River Laboratories (USA). PANC-1 cells, Chinese horseshoe

bat primary fibroblasts (bPF), mouse primary fibroblasts (mPF), and human primary fibroblasts (hPF) (1×10^6) in 100 μL of PBS containing 30% Matrigel were subcutaneously injected into three mice$^{Nu/Nu}$, respectively. Twelve mice$^{Nu/Nu}$ were used in total. After two months, tumors were detected and captured.

For *in vivo* M1001 evaluation assay, C57BL/6 mice were purchased from the Animal Facility of the Kunming Institute of Zoology, CAS. Sixteen-week-old male C57BL/6 mice were randomly assigned to different treatment group, with five mice in each group. BLM (3 U/kg body weight) was intratracheally administered to mice in groups 2 and 3. Mice in group 1 were administered by the same volume of vehicle (water). After one week, mice in groups 2 and 3 were administered vehicle (10% dimethyl sulfoxide (DMSO), 40% PEG300, 5% Tween-80, 45% saline) or M1001 (10 mg/kg) by gavage, respectively. Treatments were performed twice per week. Three weeks after treatment, the mice were sacrificed, and their lungs were collected for SA-β-gal staining. The lung tissues were digested using a mixture of 10 mg/mL collagenase, 1 mg/mL hyaluronidase, and 200 mg/mL DNase1 at 37 °C for 1 h. Single-cell suspensions were prepared, and red blood cells were lysed using ACK lysis buffer (Thermo Fisher, USA, Cat. No. A1049201) to obtain single cells for cytospinning and TIF analysis.

Statistical analysis and reproducibility

Experiments were repeated three times unless otherwise stated. All statistical analyses were conducted using GraphPad Prism v7 (GraphPad, USA). Student's *t*-test was performed to determine *P*-values of the raw data unless otherwise stated, with $P<0.05$ considered significant. Representative images are shown unless otherwise stated. Quantitative data are expressed as means±standard deviation (SD) unless otherwise stated. Imaging analysis was performed blind without knowing the experimental groups, but not randomly as different experimental groups were examined together.

RESULTS

Bat primary fibroblasts display extra-stabilized telomeres in consecutive proliferation

Based on T-FISH analysis, we observed that compared with primary fibroblasts derived from primates (macaques and humans) and rodents (rats and mice) those derived from Chinese horseshoe bats displayed giant and heterogeneous telomere foci (left panel in Supplementary Figure S1A). Similar observations were made for primary fibroblasts derived from Rickett's big-footed bats, another Chiroptera species (Supplementary Figure S1A). Indeed, when quantifying the fluorescent strength of telomeric spots, the bat fibroblasts exhibited much greater T-FISH signaling strength (Supplementary Figure S1B). The interval distribution of T-FISH spots was determined based on fluorescent strength. Unlike the curves for primate and rodent fibroblasts, with only one peak, Rickett's big-footed bat fibroblasts had two peaks, with around 40% of foci exhibiting significant T-FISH signals (Supplementary Figure S1C). These findings indicate that bat fibroblasts exhibit unique telomeric patterns.

Among the primary fibroblast cohorts, those from Rickett's big-footed bats showed the strongest T-FISH signals. We next investigated telomeric dynamics in consecutive expansion but culturing bPF, mPF, and hPF in physiological oxygen tension (2% oxygen), with passaging every 3 d. In total, cells were expanded consecutively for 60 d (around 20 passages). Cells in the first five passages were defined as early passages, while cells after 15 passages were defined as advanced (Figure 1A). Telomeric length was evaluated using quantitative T-FISH (Figure 1B) and qRT-PCR methods (Figure 1C). Compared with mPF and hPF, which displayed considerable telomeric shortening, bPF showed markedly longer telomeres and stable maintenance of telomeric length, in line with the observations in Supplementary Figure S1. In addition, based on T-FISH and anti-γH2A.X immunostaining, we observed markedly increased TIF in the advanced passages of both mPF and hPF, but consistently low levels of TIF in bPF (Figure 1D, E). These findings suggest that bat fibroblasts maintain telomeric stability during proliferation.

Oxidative DNA damage is a substantial threat to telomeric stability. In murine fibroblasts, oxidative stress is a major driver of cellular senescence (Parrinello et al., 2003). Here, we measured endogenous ROS levels using fluorogenic DCFH-DA staining combined with flow cytometry analysis. Notably, both mPF and hPF showed elevated ROS levels in advanced passages compared to their own early counterparts. In contrast, bPF cells consistently exhibited low ROS (Figure 1F, G). Additionally, bPF contained lower levels of oxidative DNA damage than mPF and hPF, as evaluated by 8-OHdG ELISA (Figure 1H).

Finally, we performed BrdU labeling to evaluate proliferation dynamics of these cells. Compared to the early passages, mPF and hPF cells in the advanced passages displayed much slower proliferation, whereas the bPF cells did not (Figure 1I). Correspondingly, more than 90% of mPF and hPF cells in advanced passages showed senescence, while only 5% of bPF cells were SA-β-gal-positive (Figure 1J, K). Consistent with SA-β-gal staining, no obvious expression of senescence markers P16, P21, and c-Fos was detected in the bPF cells, but cellular proliferation marker cyclin A remained at a high level in advanced bPF cells (Figure 1L). These findings are consistent with previous comparative studies of multiple species showing that bat skin fibroblasts exhibit prolonged population doubling (Lorenzini et al., 2005; Rohme, 1981).

The bPF cells displayed higher expression of cyclin A during the advanced passages compared to the early passages (Figure 1L). To evaluate whether spontaneous immortalization occurred in bPF cells during expansion, we carried out subcutaneous tumor formation assays using advanced bPF, mPF, and hPF cells. The PANC-1 pancreatic cancer cell line, which is capable of forming tumors, was included as an operational control. Nude mice were sacrificed 60 d post injection. Of note, no tumors were found in mice injected with bPF, mPF, or hPF cells (Supplementary Figure S2A). These findings support the notion that bat primary fibroblasts are superior for maintaining telomeric stability during long-term proliferation.

Telomere-associated genes are highly expressed in bat fibroblasts

To determine the intrinsic mechanism of bat cells, we performed transcriptome sequencing using total RNA collected from mPF and bPF at the 10th passage (Figure 2A). DEG analysis identified 238 up-regulated genes in bPF cells compared with mPF cells (fold-change>2) (Supplementary Table S5). Consistent with the cellular observations, KEGG

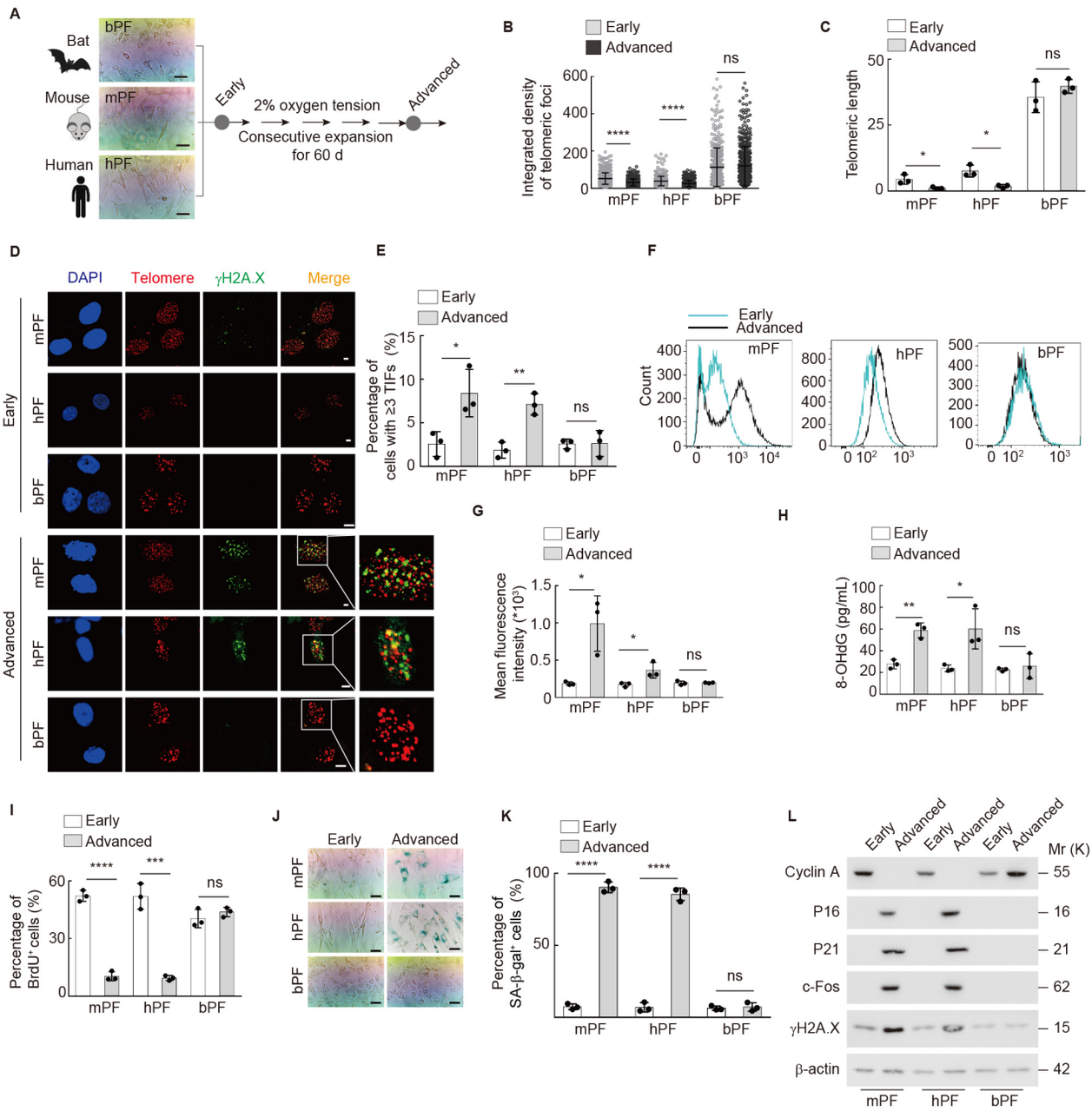

Figure 1 Bat primary fibroblasts show stabilized telomeres and resistance to replicative senescence

A: Schematic of replicative senescence comparison of bat, mouse, and human fibroblasts. B, C: Quantitative T-FISH (B) and qRT-PCR-based measurement (C) of telomere length in bPF, mPF, and hPF cells at early and advanced passages. D, E: Representative T-FISH images (D) and percentage of cells with ≥3 TIFs (E) in bPF, mPF, and hPF at early and advanced passages, respectively. Telomeric PNA probe (red) and γH2A.X (green) were used to label damaged telomeres. *n*=100 nuclei in each sample. F, G: Intracellular ROS measurement using DCFH-DA labeling and flow cytometry. Results are presented as fluorescence intensity histograms (F) and relative fluorescence levels (G). H: Quantification of 8-OHdG in early and advanced passages of bPF, mPF, and hPF cells using ELISA. I: BrdU incorporation assay of proliferation of mPF, hPF, and bPF cells at early and advanced passages. J, K: Representative images (J) and quantification (K) of SA-β-gal-positive bPF, mPF, and hPF cells at early and advanced passages. L: Immunoblotting of cellular proliferation marker cyclin A, senescence markers P16, P21, and c-Fos, and DNA damage marker γH2A.X in bPF, mPF, and hPF. β-actin was used as a loading control. *n*=3 independent experiments unless otherwise stated. Scale bar: 50 μm in A and J, 5 μm in D. Data represent mean±*SD*. *P*-values were calculated using a two-tailed student's *t*-test. ns: Not significant; *: *P*<0.05; **: *P*<0.01; ***: *P*<0.001; ****: *P*<0.0001.

analysis revealed that the cellular senescence pathway was the top ranked pathway (Supplementary Figure S2B, C and Table S6). Senescence-inhibiting genes *SIRT1*, *AKT1*, and *MYC* were up-regulated in the bPF cells. GO enrichment analysis of the bPF up-regulated genes identified pathways involved in chromosomes, telomeric region, chromatin remodeling, DNA replication, and DNA repair (Figure 2B, C; Supplementary Table S7), with the telomeric pathway ranking first. We compared the expression of these telomere-associated genes between the early and advanced passages using qRT-PCR (Supplementary Figure S3A–C). Most genes were significantly down-regulated in the advanced mPF

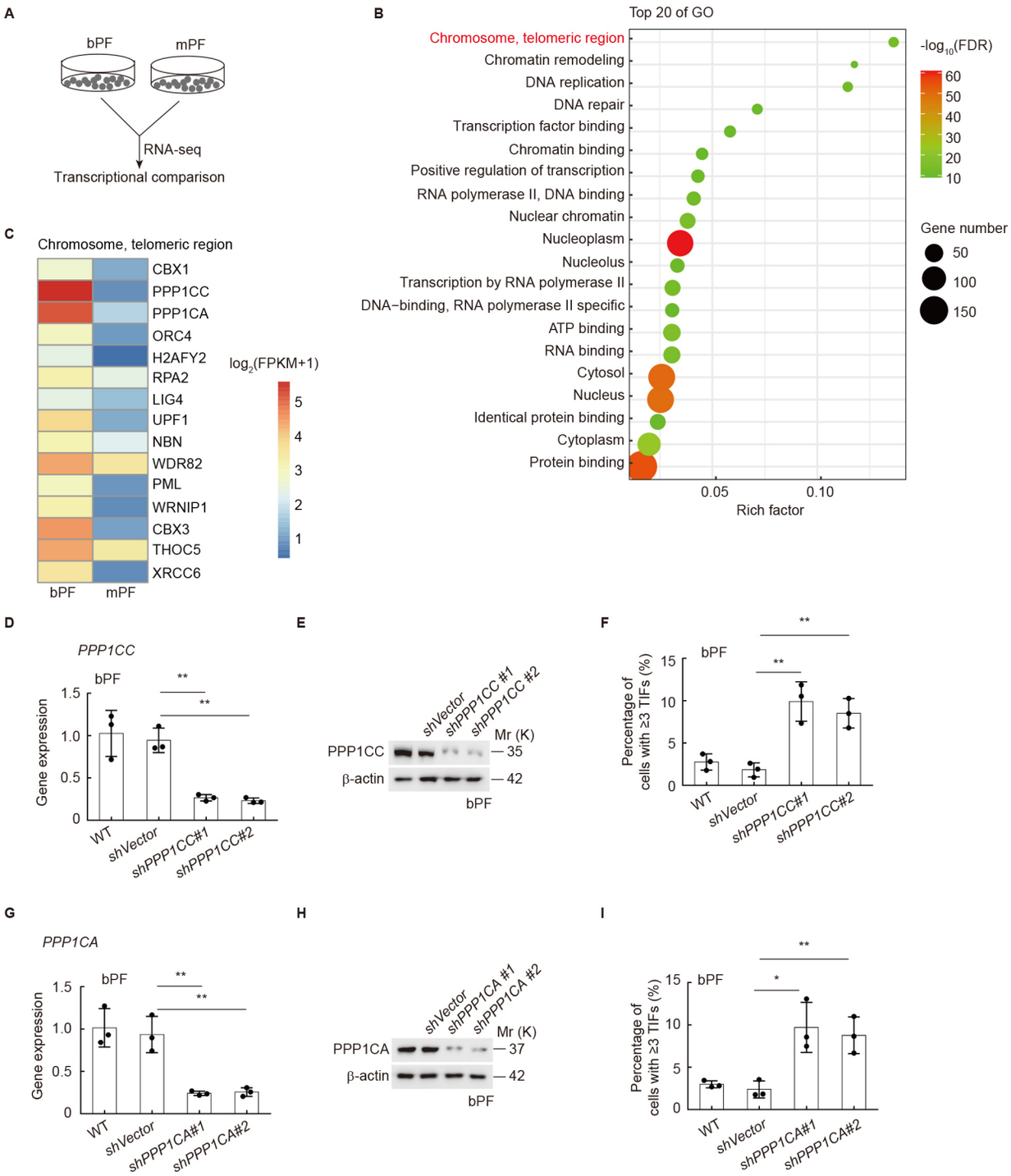

Figure 2 Telomere-associated genes are highly expressed in bat fibroblasts

A: Schematic of sample collection and RNA-seq. B: GO analysis of highly expressed genes in bPF compared with mPF (FPKM fold-change>2). Pathways were ranked based on Rich factors. C: Heatmap of enriched telomere-related genes in bPF and mPF. D, E: qRT-PCR (D) and immunoblotting (E) detection of PPP1CC expression in bPF cells with or without *PPP1CC* knockdown. F: Quantification of TIF in bPF cells with or without *PPP1CC* knockdown. G, H: qRT-PCR (G) and immunoblotting (H) detection of PPP1CA expression in bPF cells with or without *PPP1CA* knockdown. I: Quantification of TIF in bPF cells with or without *PPP1CA* knockdown. *n*=3 independent experiments unless otherwise stated. Data represent mean±*SD*. *P*-values were calculated using a two-tailed student's *t*-test. ns: Not significant; *: *P*<0.05; **: *P*<0.01; ***: *P*<0.001; ****: *P*<0.0001.

(Supplementary Figure S3A) and hPF cells (Supplementary Figure S3B) compared to their early-passage counterparts. In contrast, bPF cells showed persistent expression of these genes during expansion (Supplementary Figure S3C). These results indicate that bat fibroblasts can maintain an overall high expression of telomere-related genes during consecutive expansion.

PPP1CC and PPP1CA proteins have been identified at telomeres in HeLa cells (Déjardin & Kingston, 2009; Grolimund et al., 2013). Here, both were highly expressed in

the bPF cells (Figure 2C). The two genes were knocked down in the bPF cells, with efficiency confirmed using qRT-PCR (Figure 2D, G) and immunoblotting (Figure 2E, H). Results showed that bPF cells with *PPP1CC* or *PPP1CA* knockdown displayed markedly increased TIF (Figure 2F, I), suggesting that *PPP1CC* and *PPP1CA* play vital roles in telomeric stabilization in bPF cells. Together, these results support the notion that bat fibroblasts use classical mechanisms to protect telomeres.

Up-regulation of *EPAS1* gene in bat fibroblasts plays a key role in telomeric stability

The TelNet database contains genes associated with telomeres (http://www.cancertelsys.org/telnet/) (Supplementary Table S8), with each gene assigned a score from 1 to 10 to reflect the significance of telomeric functions. To explore specific telomeric regulators in bPF cells, we cross-referenced 54 up-regulated genes in bPF cells (fold-change>20 compared to mPF, Supplementary Table S9) with TelNet. All 54 genes were in the TelNet database (Figure 3A), including six genes with TelNet scores greater than 5 (Supplementary Figure S4A). We selected the top three genes, *SUMO2, HNRNPK*, and *EPAS1*, for validation. *SUMO2* displayed lower expression in the bPF cells than in the mPF and hPF cells (Supplementary Figure S4B), inconsistent with the RNA-seq data. *HNRNPK* displayed high expression levels of mRNA (Supplementary Figure S4C) but not protein in the bPF cells compared to the mPF and hPF cells (Supplementary Figure S4D). Of note, *EPAS1*, ranked first based on FPKM fold-changes (Supplementary Figure S4A), displayed markedly high expression levels of mRNA (Figure 3B) and protein (Figure 3C) in both early and advanced bPF cells.

EPAS1 (endothelial PAS domain protein 1, also known as *HIF-2α*) is a well-defined oxygen response gene. EPAS1 forms a heterodimeric transcription factor with its obligate partner ARNT and binds to hypoxia response elements using its DNA-reading head, thereby facilitating the expression of target genes such as *VEGF* (Hewitson & Schofield, 2004). To determine the functions of EPAS1 in telomeric stability, we knocked down *EPAS1* in the bPF cells (Supplementary Figure S4E, S4G). *EPAS1* knockdown caused substantial TIF accumulation (Figure 3D). A similar observation was made using PT2385 to specifically target EPAS1-ARNT interactions to inhibit transcription factor activities (Figure 3E, F) (Wu et al., 2019). These findings indicate that the functions of EPAS1 in telomeric protection depend on its transcriptional regulation activities. In addition, PT2385 treatment did not change the telomeric pattern in bPF cells (Supplementary Figure S4H), but sensitized bPF cells to oxidative DNA damage (Figure 3G). Furthermore, bPF cells cultured with PT2385 displayed significant senescence, as determined by SA-β-gal staining and immunoblotting targeting p16 and p21 (Figure 3H–J).

In contrast to PT2385, the M1001 agonist targeted EPAS1-ARNT interactions to promote their transcriptional regulatory activity (Figure 3K). To validate the function of EPAS1 in telomeric protection, we treated senescence-sensitive mPF cells with M1001. Consecutive expansion was repeated with the addition of M1001 in the culture medium. Under these conditions, mPF cells displayed low oxidative DNA damage (Figure 3L), low TIF rates (Figure 3M), and senescence resistance (Figure 3N, O) even in advanced passages. To confirm the on-targeting of M1001, we repeated the same treatment in *EPAS1*-knockdown mPF cells (Supplementary Figure S4F, G). Indeed, *EPAS1* knockdown diminished the telomeric protective effects of M1001 (Figure 3M). *EPAS1* knockdown in mPF cells produced senescence even under M1001 treatment (Figure 3N, O). We also examined the expression and functions of ARNT in telomeric protection. Likewise, ARNT expression was significantly decreased in mPF and hPF cells during consecutive passaging but remained consistently high in bPF cells (Supplementary Figure S4I). *ARNT* knockdown in bPF cells resulted in a phenotype similar to the accumulation of TIF observed under *EPAS1* down-regulation or activity inhibition conditions (Supplementary Figure S4J, K, L). Thus, these findings support the notion that EPAS1 plays a key role in telomeric stability through its transcriptional regulatory activities.

EPAS1 promotes *TRF1*, *TRF2*, and *RAD50* transcription

To determine the mechanisms underlying telomeric stabilization by EPAS1, we performed co-immunostaining of EPAS1 and T-FISH spots in bPF and mPF cells. No obvious localization of EPAS1 was detected in the telomeric spots (Supplementary Figure S5A). Likewise, EPAS1 did not co-localize with the DNA damage sites, as indicated by γH2A.X (Supplementary Figure S5B). As a transcription factor, EPAS1 binds to the conserved CACGT motif in the TSS of its target genes (Supplementary Figure S5C) (Zheng et al., 2019). We selected 10 genes with a TelNet score>9 for screening (Supplementary Figure S5D), with *VEGF* established as a positive control. All genes contained the CACGT motif in their TSS regions (Supplementary Figure S5E). The mPF cells were treated with vehicle, PT2385, or M1001, respectively, and mRNA was purified for qRT-PCR analysis. Among the genes, *TERT* was below the detectable level (data not shown). Neither PT2385 (P=0.2211) nor M1001 (P=0.0541) changed the expression of *STN1* (Supplementary Figure S5F). The expression levels of *POT1*, *TRF2IP*, *TINF2*, *ACD*, and *NBN* did not change under PT2385 treatment, but were up-regulated by M1001 (Supplementary Figure S5G–K). *PML* was down-regulated by PT2385 (P=0.0011) but showed no change under M1001 treatment (P=0.3239) (Supplementary Figure S5L). Notably, the expression levels of *TRF1*, *TRF2*, and *RAD50* were dependent on EPAS1 activity. As shown in Figure 4A–C, the expression levels of *TRF1*, *TRF2*, and *RAD50* were inhibited by PT2385 (P=0.0041, P=0.0012, and P=0.0040, respectively) but promoted by M1001 (P=0.0152, P=0.0051, and P=0.0004, respectively).

Luciferase reporter assays were performed for further validation (Figure 4D). Promoter regions of *TRF1*, *TRF2*, *RAD50*, and *VEGF* (1 000 bp upstream from TSS; Supplementary Table S2) were constructed into pGL4.11 vectors. The vectors were transfected into mPF cells with or without *EPAS1* knockdown. Results showed that *EPAS1* knockdown significantly reduced the luminescence strength of *TRF1* (Figure 4E), *TRF2* (Figure 4F), *RAD50* (Figure 4G), and *VEGF* (positive control) (Figure 4H). In addition, immunoblotting revealed that the protein abundance of these three factors in mPF cells was dependent on the transcriptional activity of EPAS1 (Figure 4I). Consistently, TRF1, TRF2, and RAD50 levels were down-regulated in advanced passages of mPF and hPF cells but remained consistently high in the bPF cells (Figure 4J). We also explored the correlation between *EPAS1* expression and *TRF1*, *TRF2*, and *RAD50* in human tissues. Pearson

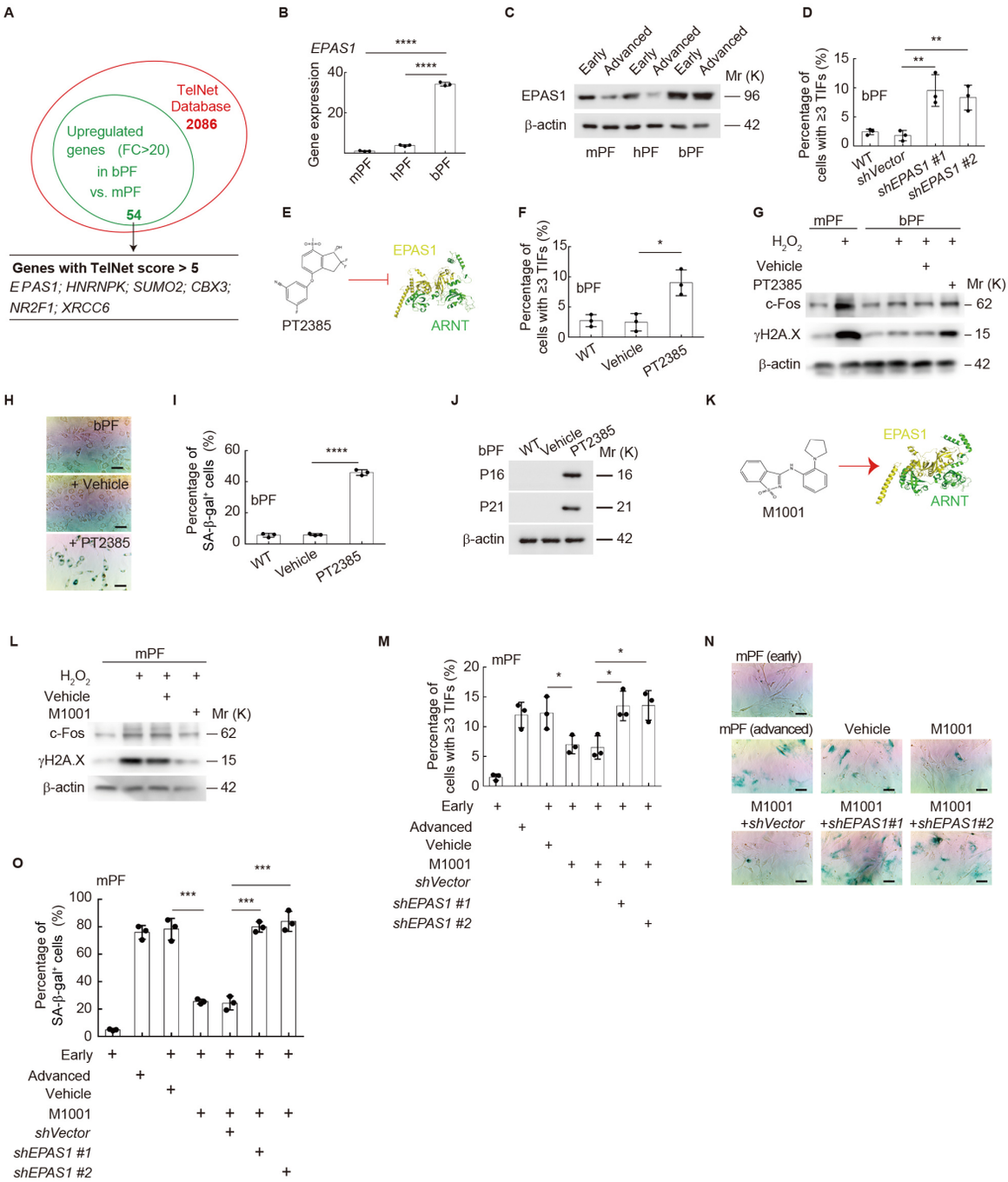

Figure 3 EPAS1 promotes telomeric stabilization based on its transcriptional activity

A: Cross-referencing identification of potential telomeric protection factors in bPF. B: qRT-PCR-based transcriptional comparison of *EPAS1* in bPF, mPF, and hPF. C: Immunoblotting of EPAS1 in bPF, mPF, and hPF at early and advanced passages, respectively. β-actin was used as a loading control. D: Quantification of cells with ≥3 TIFs in bPF with or without *EPAS1* knockdown. In total, 100 cells were analyzed for each sample. E: EPAS1 antagonist PT2385 inhibited EPAS1 and ARNT interactions and decreased EPAS1 transcriptional activity. F: Quantification of cells with ≥3 TIFs in bPF under vehicle or 10 μmol/L PT2385 treatment for 7 d. In total, 100 cells were analyzed for each sample. G: Immunoblotting of γH2A.X and c-Fos in mPF and bPF. Cells were treated with 400 μmol/L H_2O_2 for 2 h, followed by culture for 7 d with or without 10 μmol/L PT2385. β-actin was used as a loading control. H, I: Representative images (H) and quantification (I) of SA-β-gal-positive bPF cells under vehicle or 10 μmol/L PT2385 treatment for 7 d. J: Immunoblotting of p16 and p21 in bPF cells under vehicle or 10 μmol/L PT2385 treatment for 7 d. β-actin was used as a loading control. K: EPAS1 agonist M1001 stabilized EPAS1 and ARNT interactions and promoted EPAS1 transcriptional activity. L: Immunoblotting of γH2A.X and c-Fos in mPF under H_2O_2 treatment. Cells were treated with 400 μmol/L H_2O_2 for 2 h, followed by culture for 7 d with or without 10 μmol/L M1001. β-actin was used as a loading control. M: Quantification of cells with ≥3 TIFs in mPF with or without EPAS1 knockdown under vehicle or 10 μmol/L M1001 treatment for 7 d. In total, 100 cells were analyzed for each sample. N, O: Representative images (N) and quantification (O) of SA-β-gal-positive mPF cells with or without EPAS1 knockdown under vehicle or 10 μmol/L M1001 treatment for 7 d. *n*=3 independent experiments unless otherwise stated. Scale bar: 50 μm. Data represent mean±*SD*. *P*-values were calculated using a two-tailed student's *t*-test. ns: Not significant; *: $P<0.05$; **: $P<0.01$; ***: $P<0.001$; ****: $P<0.0001$.

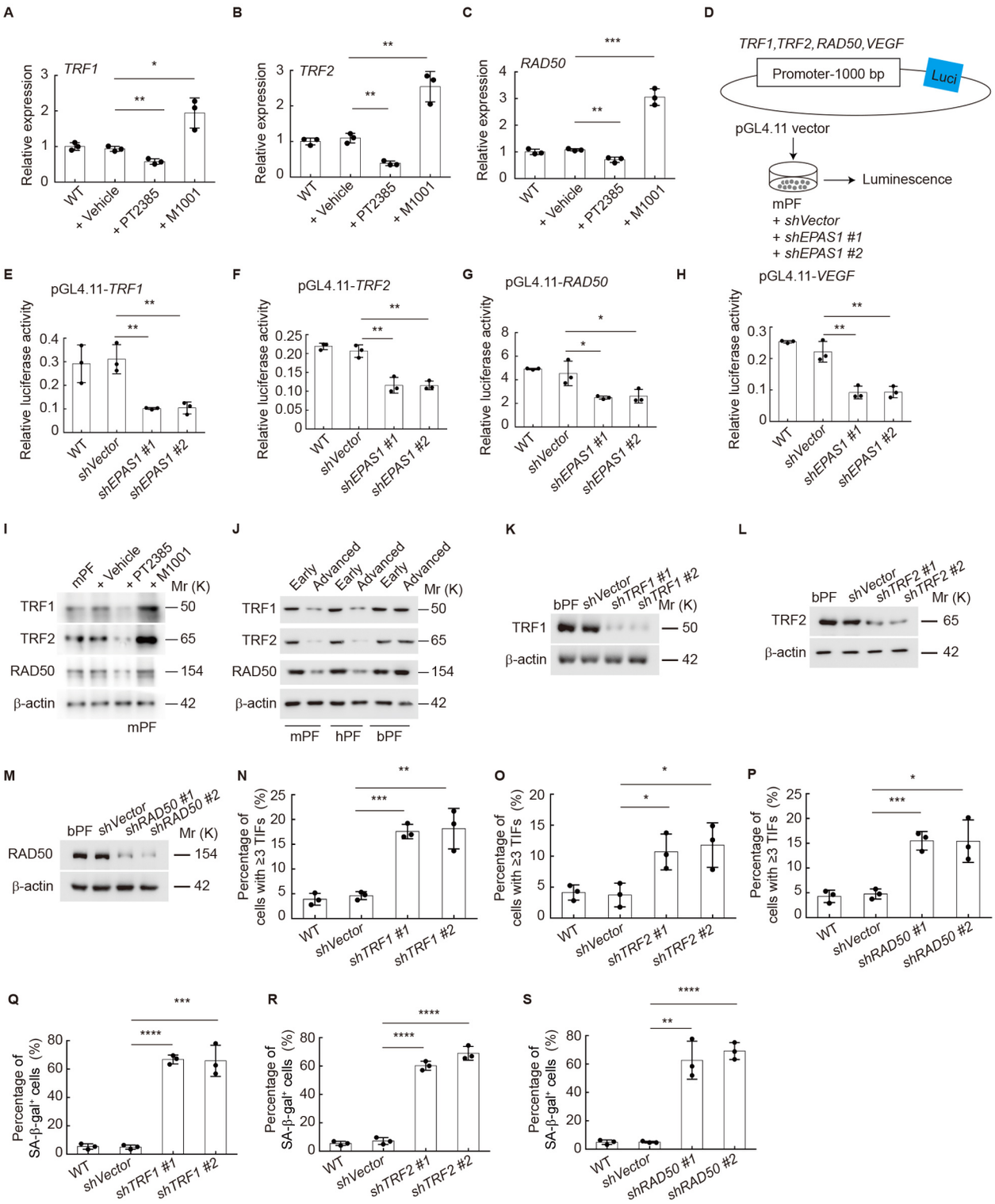

Figure 4 EPAS1 promotes *TRF1*, *TRF2*, and *RAD50* transcription

A–C: qRT-PCR-based transcriptional comparison of *TRF1* (A), *TRF2* (B), and *RAD50* (C) in mPF under vehicle, 10 μmol/L PT2385, or 10 μmol/L M1001 treatment for 2 d. D–H: Diagram of luciferase (Luci) reporter assay (D) for analysis of transcriptional regulation of EPAS1 on *TRF1* (E), *TRF2* (F), and *RAD50* (G). *VEGF* was used as a positive control (H). I: Immunoblotting of TRF1, TRF2, and RAD50 in mPF under vehicle, 10 μmol/L PT2385, or 10 μmol/L M1001 treatment for 2 d. β-actin was used as a loading control. J: Immunoblotting of TRF1, TRF2, and RAD50 in bPF, mPF, and hPF cells at early and advanced passages, respectively. β-actin was used as a loading control. K: Immunoblotting of TRF1 in bPF cells with or without *TRF1* knockdown. L: Immunoblotting of TRF2 in bPF cells with or without *TRF2* knockdown. M: Immunoblotting of RAD50 in bPF cells with or without *RAD50* knockdown. N–P: Quantification of cells with ≥3 TIFs in bPF cells with *TRF1* knockdown (N), *TRF2* knockdown (O), and *RAD50* knockdown (P). In total, 100 cells were analyzed for each sample. Q–S: Quantification of SA-β-gal-positive bPF cells with *TRF1* knockdown (Q), *TRF2* knockdown (R), and *RAD50* knockdown (S). *n*=3 independent experiments unless otherwise stated. Data represent mean±*SD*. *P*-values were calculated using a two-tailed student's *t*-test. ns: Not significant; *: $P<0.05$; **: $P<0.01$; ***: $P<0.001$; ****: $P<0.0001$.

correlation analysis revealed positive correlations between *EPAS1* and the three telomeric genes in human normal lung tissues (Supplementary Figure S5M–O). To confirm the telomeric protective roles of *TRF1*, *TRF2*, and *RAD50*, we knocked down each of these genes in the bPF cells (Figure 4K–M). Notably, down-regulation of each gene increased the TIF rates (Figure 4N–P) and percentage of SA-β-gal-positive cells (Figure 4Q–S) in the bPF cells. Thus, these findings support the notion that EPAS1 promotes *TRF1*, *TRF2*, and *RAD50* transcription.

EPAS1 agonist M1001 attenuates BLM-induced senescence in human pulmonary endothelial cells

To investigate the functional conservation of EPAS1 in humans, we examined the expression of *EPAS1* in major human organs and tissues. Among the major organs, the expression of *EPAS1* was highest in the lung (Supplementary Figure S6A). We further examined the single-cell transcriptome atlas of the human lung from the CZ CELLxGENE database (https://cellxgene.cziscience.com/). Among the single-cell subpopulations, the expression of *EPAS1* was highest in the pulmonary endothelial cells (Supplementary Figure S6B, C). Focusing on this population, *EPAS1* expression remaining stable before 60 years old, decreased markedly between 60–70 years old, and subsequently recovered after 70 years old (Figure 5A). We then examined the expression dynamics of the three target genes. *RAD50* transcription was not detected in this dataset. Of note, similar patterns were observed for *TRF1* and *TRF2* (Figure 5B, C). Compared to the 50–60-year-old group, *TRF1* was significantly down-regulated (P=2.24e10^{-7}) and *TRF2* was slightly down-regulated (P=0.057) in the 60–70-year-old group, consistent with *EPAS1* transcriptional dynamics. Pearson correlation analysis also revealed a positive correlation between *EPAS1* and *TRF1* (Supplementary Figure S6D), as well as *EPAS1* and *TRF2* (Supplementary Figure S6E), in the human pulmonary endothelial cells. We used *in vitro*-cultured human pulmonary endothelial cell line HLF-α and immunoblotting for validation (Supplementary Figure S6F). Consistently, TRF1, TRF2, and RAD50 were down-regulated in the HLF-α cells under PT2385 treatment, but up-regulated under M1001 treatment (Figure 5D).

Finally, we tested the protective effects of M1001 in the context of BLM-induced telomeric damage and senescence. To this goal, the HLF-α cells were treated with BLM for 16 h, followed by extended culture with or without M1001 for 7 d (Figure 5E). *EPAS1* knockdown groups were included for further validation of the M1001 on-targeting effects in human cells (Supplementary Figure S6G, H). M1001 attenuated the BLM-induced TIF rates (Figure 5F) and percentage of SA-β-gal-positive cells (Figure 5G, H). Likewise, SASP factor expression was also suppressed by M1001 treatment (Supplementary Figure S7). We further used a BLM-induced pulmonary damage mouse model to evaluate the physiological protective effects of M1001 (Figure 5I). Consistently, M1001 attenuated BLM-induced senescence (Figure 5J) and telomeric damage (Figure 5K, L). Thus, these findings suggest that EPAS1 agonist M1001 attenuates BLM-induced telomeric damage and senescence (Figure 5M).

DISCUSSION

Although blood transcriptome analysis has indicated that long-lived bat species have longer and more stable telomeres (Foley et al., 2018), the underlying mechanisms behind these phenomena remain unknown. In this study, we provided evidence supporting EPAS1 as a key regulator promoting the transcription of shelterin components TRF1 and TRF2, as well as the DNA repair gene *RAD50*. High expression of EPAS1 in bat fibroblasts conferred resistance to senescence during consecutive passaging, consistent with reports that bats show little to no evidence of senescence (Fleischer et al., 2017). Furthermore, in addition to the three confirmed genes, other telomere-related genes, including *POT1*, *TRF2IP*, *TINF2*, *ACD*, and *NBN*, were up-regulated in response to M1001 treatment. These findings suggest that EPAS1 may have broader effects in telomere stabilization. While human fibroblasts are sensitive to telomeric attrition-induced senescence, murine fibroblasts are sensitive to oxidative DNA damage-induced senescence (Parrinello et al., 2003). In our system, we observed significant telomeric damage in murine fibroblasts at advanced passages. Oxidative stress can induce systematic genome damage, including telomere dysfunction, in a time-dependent manner (De Rosa et al., 2021). Furthermore, key factors, such as RAD50, function in many aspects of genomic integrity. RAD50 can cooperate with MRE11 and NBS1 to amplify DNA damage signaling, as well as interact with TRF2 and localize on telomeres (Zhu et al., 2000), consistent with the network model of genomic stability regulation.

Age estimation is a major challenge in studies of wild animals, including bats (Power et al., 2021). One limitation of this study is the lack of exact age information for the bats used in fibroblast derivation. Notably, various weather conditions, such as temperature, rainfall, and wind speed, have been linked to changes in longitudinal telomere dynamics in bats (Foley et al., 2020). Given that oxygen concentration is another major component of weather conditions and *EPAS1* is a well-defined oxygen response gene, we propose that hypoxia should be considered in future studies investigating bat longevity. (Foley et al., 2018) previously suggested the potential importance of ALT in telomeric maintenance in bats. Consistently, we observed very large and heterogeneous telomeric foci in the studied bat cells, typical characteristics of ALT. This morphological evidence highlights the need for further experimental validation of ALT mechanisms in bats. While the mechanisms of ALT have been explored in cancer systems, such as sarcoma (Eastley et al., 2017), bat cells may serve as a novel system for ALT study.

Various strategies have been developed to mitigate the detrimental effects of senescence, either through senescence elimination by senolytics (Kang, 2019) or suppression of SASP by senomorphics (Lagoumtzi and Chondrogianni, 2021). The lung is an aging-sensitive organ (Yousefzadeh et al., 2020) and several lung diseases are associated with telomere dysfunction (Rossiello et al., 2022). In the current study, we presented evidence supporting the effectiveness of the EPAS1 agonist M1001 in preventing senescence in human pulmonary diseases. Notably, based on single-cell transcriptome analysis, EPAS1 expression in human pulmonary endothelial cells was down-regulated in 60–70-year-old populations, but recovered in 70-year-old populations. These findings indicate that EPAS1 may be dynamically regulated in the context of different physiological states, which needs to be clarified and considered in the potential anti-aging application of M1001.

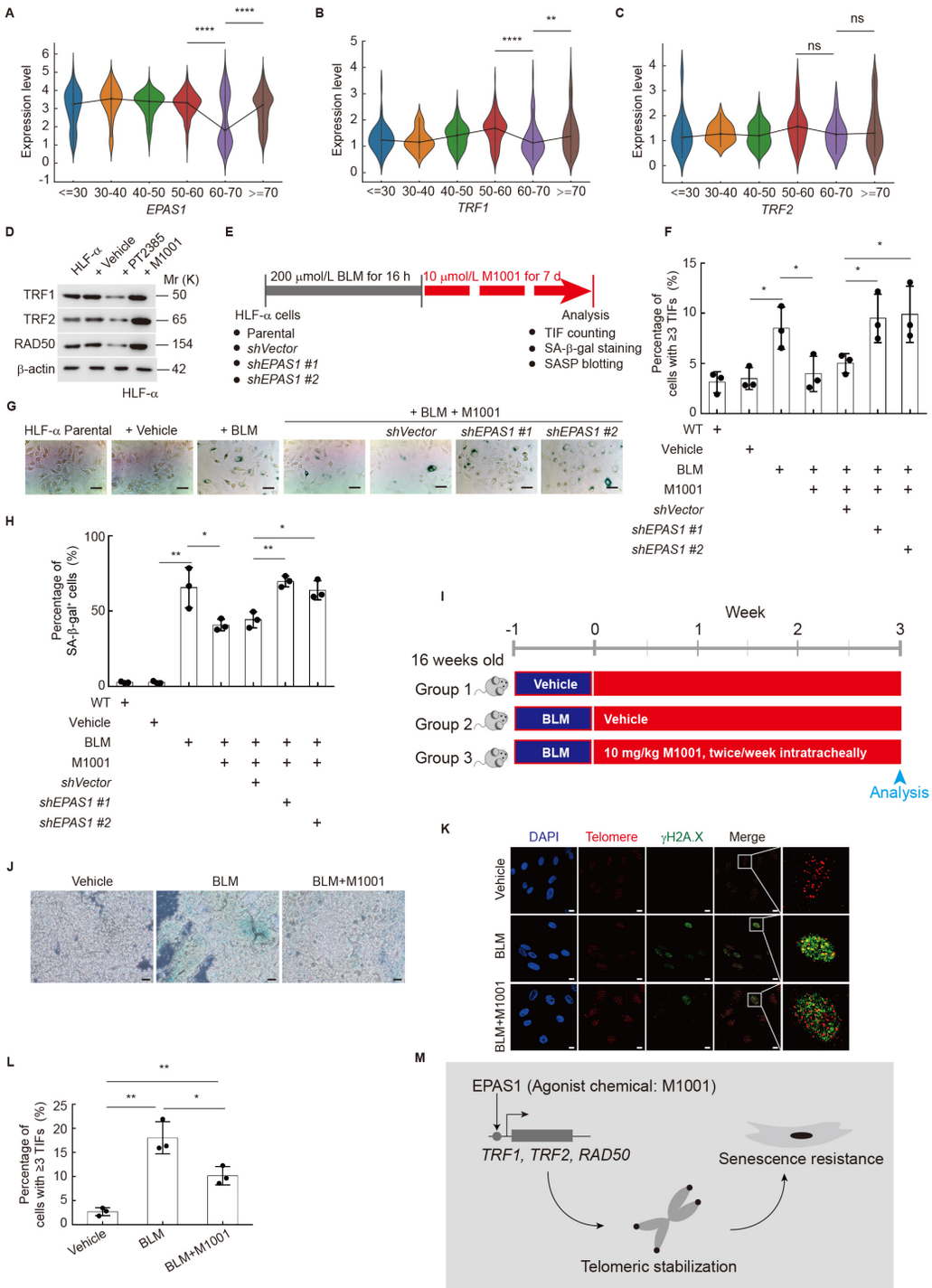

Figure 5 M1001 attenuates BLM-induced telomeric damage and senescence in human pulmonary endothelial cells

A–C: Transcriptional dynamics of *EPAS1* (A), *TRF1* (B), and *TRF2* (C) in human pulmonary endothelial cell subpopulations. Results were re-analyzed using a human lung single-cell transcriptome atlas. *P*-values were calculated using Mann-Whitney U test (two-sided). D: Immunoblotting of TRF1, TRF2, and RAD50 in HLF-α cells under vehicle, 10 μmol/L PT2385, or 10 μmol/L M1001 treatment for 2 d. β-actin was used as a loading control. E: Experimental design of BLM and M1001 treatment in HLF-α cells. F: Quantification of cells with ≥3 TIFs in HLF-α with or without *EPAS1* knockdown. Cells were pretreated with vehicle or 200 μmol/L BLM for 16 h, followed by culture with 10 μmol/L M1001 for 7 d. In total, 100 cells were analyzed in each sample. G, H: Representative images (G) and quantification (H) of SA-β-gal-positive HLF-α cells with or without *EPAS1* knockdown. Cells were pretreated with vehicle or 200 μmol/L BLM for 16 h, followed by culture with 10 μmol/L M1001 for 7 d. In total, 200 cells were analyzed in each sample. I: Experimental design of BLM (3 U/kg body weight)-induced pulmonary damage in adult mice, combined with or without M1001 (10 mg/kg body weight) treatment. J: SA-β-gal staining in mouse lung biopsies. K, L: Representative images (K) and quantification (L) of cells with ≥3 TIFs in mouse lung single cells. Mouse lung was digested into single cells, and cells were cytospun onto slides for T-FISH combined with anti-γH2A.X immunostaining and TIF counting. In total, 100 cells were analyzed in each sample. M: Graphic summary of the study. *n*=3 independent experiments unless otherwise stated. Scale bar: 50 μm in G, 100 μm in J, 10 μm in K. Data represent mean±*SD*. *P*-values were calculated using a two-tailed student's *t*-test. ns: Not significant; *: $P<0.05$; **: $P<0.01$; ***: $P<0.001$; ****: $P<0.0001$.

DATA AVAILABILITY

The RNA-seq data are available at the NCBI Gene Expression Omnibus (GEO) under accession No. SRR18461285–90, GSA at the National Genomics Data Center under accession No. PRJCA015594, and Science Data Bank under DOI: 10.57760/sciencedb.07762. All other data supporting the findings of this study are available from the corresponding author upon reasonable request.

SUPPLEMENTARY DATA

Supplementary data to this article can be found online.

COMPETING INTERESTS

B.Z. and K.Q.L. are co-inventors of a patent application covering the use of EPAS1 agonists to stabilize telomeres *in vivo* and benefit health span. All other authors declare no competing interests.

AUTHORS' CONTRIBUTIONS

K.Q.L., X.Y.L., Q.F.C., X.Y.H., Q.T., J.Z., Q.C., Y.H.X., and R.H. performed the experiments and analyzed the data. G.J.L., D.M.X., and Z.L. performed the bioinformatics and statistical analyses. B.Z. and K.Q.L. designed the experiments. B.Z. supervised the studies. B.Z. and K.Q.L. wrote the paper. B.Z. conceived the study. All authors read and approved the final version of the manuscript.

ACKNOWLEDGEMENTS

The authors would like to thank the Animal Facility at the Kunming Institute of Zoology, Chinese Academy of Sciences, for assistance in animal assays.

REFERENCES

Azzalin CM, Reichenbach P, Khoriauli L, et al. 2007. Telomeric repeat-containing RNA and RNA surveillance factors at mammalian chromosome ends. *Science*, **318**(5851): 798−801.

Bilaud T, Brun C, Ancelin K, et al. 1997. Telomeric localization of TRF2, a novel human telobox protein. *Nature Genetics*, **17**(2): 236−239.

Broccoli D, Smogorzewska A, Chong L, et al. 1997. Human telomeres contain two distinct Myb-related proteins, TRF1 and TRF2. *Nature Genetics*, **17**(2): 231−235.

Casteel DE, Zhuang SH, Zeng Y, et al. 2009. A DNA polymerase-α·primase cofactor with homology to replication protein A-32 regulates DNA replication in mammalian cells. *Journal of Biological Chemistry*, **284**(9): 5807−5818.

Cawthon RM. 2002. Telomere measurement by quantitative PCR. *Nucleic Acids Research*, **30**(10): e47.

Celli GB, Denchi EL, De Lange T. 2006. Ku70 stimulates fusion of dysfunctional telomeres yet protects chromosome ends from homologous recombination. *Nature Cell Biology*, **8**(8): 885−890.

Cesare AJ, Reddel RR. 2010. Alternative lengthening of telomeres: models, mechanisms and implications. *Nature Reviews Genetics*, **11**(5): 319−330.

Chen LY, Redon S, Lingner J. 2012. The human CST complex is a terminator of telomerase activity. *Nature*, **488**(7412): 540−544.

De Lange T. 2005. Shelterin: the protein complex that shapes and safeguards human telomeres. *Genes & Development*, **19**(18): 2100−2110.

De Rosa M, Johnson SA, Opresko PL. 2021. Roles for the 8-oxoguanine DNA repair system in protecting telomeres from oxidative stress. *Frontiers in Cell and Developmental Biology*, **9**: 758402.

Déjardin J, Kingston RE. 2009. Purification of proteins associated with specific genomic loci. *Cell*, **136**(1): 175−186.

Diala I, Wagner N, Magdinier F, et al. 2013. Telomere protection and TRF2 expression are enhanced by the canonical Wnt signalling pathway. *EMBO Reports*, **14**(4): 356−363.

Dinami R, Ercolani C, Petti E, et al. 2014. miR-155 drives telomere fragility in human breast cancer by targeting TRF1. *Cancer Research*, **74**(15): 4145−4156.

Dong WJ, Shen RZ, Wang Q, et al. 2009. Sp1 upregulates expression of TRF2 and TRF2 inhibition reduces tumorigenesis in human colorectal carcinoma cells. *Cancer Biology & Therapy*, **8**(22): 2165−2173.

Eastley N, Ottolini B, Garrido C, et al. 2017. Telomere maintenance in soft tissue sarcomas. *Journal of Clinical Pathology*, **70**(5): 371−377.

Fleischer T, Gampe J, Scheuerlein A, et al. 2017. Rare catastrophic events drive population dynamics in a bat species with negligible senescence. *Scientific Reports*, **7**(1): 7370.

Foley NM, Hughes GM, Huang ZX, et al. 2018. Growing old, yet staying young: the role of telomeres in bats' exceptional longevity. *Science Advances*, **4**(2): eaao0926.

Foley NM, Petit EJ, Brazier T, et al. 2020. Drivers of longitudinal telomere dynamics in a long-lived bat species. *Myotis myotis. Molecular Ecology*, **29**(16): 2963−2977.

Fujita K, Horikawa I, Mondal AM, et al. 2010. Positive feedback between p53 and TRF2 during telomere-damage signalling and cellular senescence. *Nature Cell Biology*, **12**(12): 1205−1212.

Gomes NMV, Ryder OA, Houck ML, et al. 2011. Comparative biology of mammalian telomeres: hypotheses on ancestral states and the roles of telomeres in longevity determination. *Aging Cell*, **10**(5): 761−768.

Grolimund L, Aeby E, Hamelin R, et al. 2013. A quantitative telomeric chromatin isolation protocol identifies different telomeric states. *Nature Communications*, **4**: 2848.

Hewitson KS, Schofield CJ. 2004. The HIF pathway as a therapeutic target. *Drug Discovery Today*, **9**(16): 704−711.

Kang C. 2019. Senolytics and senostatics: a two-pronged approach to target cellular senescence for delaying aging and age-related diseases. *Molecules and Cells*, **42**(12): 821−827.

Kim MK, Kang MR, Nam HW, et al. 2008. Regulation of telomeric repeat binding factor 1 binding to telomeres by casein kinase 2-mediated phosphorylation. *Journal of Biological Chemistry*, **283**(20): 14144−14152.

Koh J, Itahana Y, Mendenhall IH, et al. 2019. ABCB1 protects bat cells from DNA damage induced by genotoxic compounds. *Nature Communications*, **10**(1): 2820.

Lagoumtzi SM, Chondrogianni N. 2021. Senolytics and senomorphics: Natural and synthetic therapeutics in the treatment of aging and chronic diseases. *Free Radical Biology and Medicine*, **171**: 169−190.

Lei M, Podell ER, Cech TR. 2004. Structure of human POT1 bound to telomeric single-stranded DNA provides a model for chromosome end-protection. *Nature Structural & Molecular Biology*, **11**(12): 1223−1229.

Lim CJ, Cech TR. 2021. Shaping human telomeres: from shelterin and CST complexes to telomeric chromatin organization. *Nature Reviews Molecular Cell Biology*, **22**(4): 283−298.

Limbo O, Yamada Y, Russell P. 2018. Mre11-Rad50-dependent activity of ATM/Tel1 at DNA breaks and telomeres in the absence of Nbs1. *Molecular Biology of the Cell*, **29**(11): 1389−1399.

Loayza D, De Lange T. 2003. POT1 as a terminal transducer of TRF1 telomere length control. *Nature*, **423**(6943): 1013−1018.

Lorenzini A, Tresini M, Austad SN, et al. 2005. Cellular replicative capacity correlates primarily with species body mass not longevity. *Mechanisms of Ageing and Development*, **126**(10): 1130−1133.

Luo ZH, Feng XY, Wang HL, et al. 2015. Mir-23a induces telomere dysfunction and cellular senescence by inhibiting TRF2 expression. *Aging Cell*, **14**(3): 391−399.

Martínez P, Blasco MA. 2010. Role of shelterin in cancer and aging. *Aging Cell*, **9**(5): 653−666.

Mendez-Bermudez A, Hidalgo-Bravo A, Cotton VE, et al. 2012. The roles of WRN and BLM RecQ helicases in the alternative lengthening of telomeres. *Nucleic Acids Research*, **40**(21): 10809−10820.

O'Connor MS, Safari A, Xin HW, et al. 2006. A critical role for TPP1 and TIN2 interaction in high-order telomeric complex assembly. *Proceedings of*

the National Academy of Sciences of the United States of America, **103**(32): 11874−11879.

Parrinello S, Samper E, Krtolica A, et al. 2003. Oxygen sensitivity severely limits the replicative lifespan of murine fibroblasts. *Nature Cell Biology*, **5**(8): 741−747.

Power ML, Foley NM, Jones G, et al. 2021. Taking flight: an ecological, evolutionary and genomic perspective on bat telomeres. *Molecular Ecology*, **31**(23): 6053−6068.

Rai R, Chen Y, Lei M, et al. 2016. TRF2-RAP1 is required to protect telomeres from engaging in homologous recombination-mediated deletions and fusions. *Nature Communications*, **7**: 10881.

Ribes-Zamora A, Indiviglio SM, Mihalek I, et al. 2013. TRF2 Interaction with Ku Heterotetramerization Interface Gives Insight into c-NHEJ Prevention at Human Telomeres. *Cell Reports*, **5**(1): 194−206.

Rohme D. 1981. Evidence for a relationship between longevity of mammalian species and life spans of normal fibroblasts *in vitro* and erythrocytes *in vivo*. *Proceedings of the National Academy of Sciences of the United States of America*, **78**(8): 5009–5013.

Ropio J, Chebly A, Ferrer J, et al. 2020. Reliable blood cancer cells' telomere length evaluation by qPCR. *Cancer Medicine*, **9**(9): 3153−3162.

Rossiello F, Jurk D, Passos JF, et al. 2022. Telomere dysfunction in ageing and age-related diseases. *Nature Cell Biology*, **24**(2): 135−147.

Sfeir A, Kabir S, Van Overbeek M, et al. 2010. Loss of rap1 induces telomere recombination in the absence of NHEJ or a DNA damage signal. *Science*, **327**(5973): 1657−1661.

Sfeir A, Kosiyatrakul ST, Hockemeyer D, et al. 2009. Mammalian telomeres resemble fragile sites and require TRF1 for efficient replication. *Cell*, **138**(1): 90−103.

Van Steensel B & De Lange T. 1997. Control of telomere length by the human telomeric protein TRF1. *Nature*, **385**(6618): 740−743.

Van Steensel B, Smogorzewska A, De Lange T. 1998. TRF2 protects human telomeres from end-to-end fusions. *Cell*, **92**(3): 401−413.

Walker JR, Zhu XD. 2012. Post-translational modifications of TRF1 and TRF2 and their roles in telomere maintenance. *Mechanisms of Ageing and Development*, **133**(6): 421−434.

Wilkinson GS, Adams DM. 2019. Recurrent evolution of extreme longevity in bats. *Biology Letters*, **15**(4): 20180860.

Wu DL, Su XY, Lu JP, et al. 2019. Bidirectional modulation of HIF-2 activity through chemical ligands. *Nature Chemical Biology*, **15**(4): 367−376.

Wu S, Ge YL, Li XC, et al. 2020. BRM-SWI/SNF chromatin remodeling complex enables functional telomeres by promoting co-expression of TRF2 and TRF1. *PLoS Genetics*, **16**(6): e1008799.

Yousefzadeh MJ, Zhao J, Bukata C, et al. 2020. Tissue specificity of senescent cell accumulation during physiologic and accelerated aging of mice. *Aging Cell*, **19**(3): e13094.

Zheng RB, Wan CX, Mei SL, et al. 2019. Cistrome data browser: expanded datasets and new tools for gene regulatory analysis. *Nucleic Acids Research*, **47**(D1): D729−D735.

Zhu XD, Küster B, Mann M, et al. 2000. Cell-cycle-regulated association of RAD50/MRE11/NBS1 with TRF2 and human telomeres. *Nature Genetics*, **25**(3): 347−352.

ZR | Zoological Research

Supplementary Materials

EPAS1 prevents telomeric damage-induced senescence by enhancing transcription of *TRF1*, *TRF2*, and *RAD50*

Kai-Qin Li[1,#], Gao-Jing Liu[1,#], Xiu-Yun Liu[1,3,#], Qiong-Fang Chen[1,#], Xiao-Yan Huang[1,3,#], Qiu Tu[1], Jiao Zhang[1], Qing Chang[1,4], Yun-Hua Xie[1,4], Rong Hua[1,2], Dong-Ming Xu[1,2], Zhen Liu[1,2], Bo Zhao[1,4,*]

[1] Key Laboratory of Animal Models and Human Disease Mechanisms of the Chinese Academy of Sciences & Yunnan Province, KIZ-CUHK Joint Laboratory of Bioresources and Molecular Research in Common Diseases, Kunming Institute of Zoology, Chinese Academy of Sciences, Kunming, Yunnan 650201, China
[2] State Key Laboratory of Genetic Resources and Evolution, Kunming Institute of Zoology, Chinese Academy of Sciences, Kunming, Yunnan 650201, China
[3] University of Chinese Academy of Sciences, Beijing 100049, China
[4] Primate Facility, National Research Facility for Phenotypic & Genetic Analysis of Model Animals, and National Resource Center for Non-Human Primates, Kunming Institute of Zoology, Chinese Academy of Sciences, Kunming, Yunnan 650201, China

[#]Authors contributed equally to this work
[*]Corresponding author, E-mail: zhaobo@mail.kiz.ac.cn

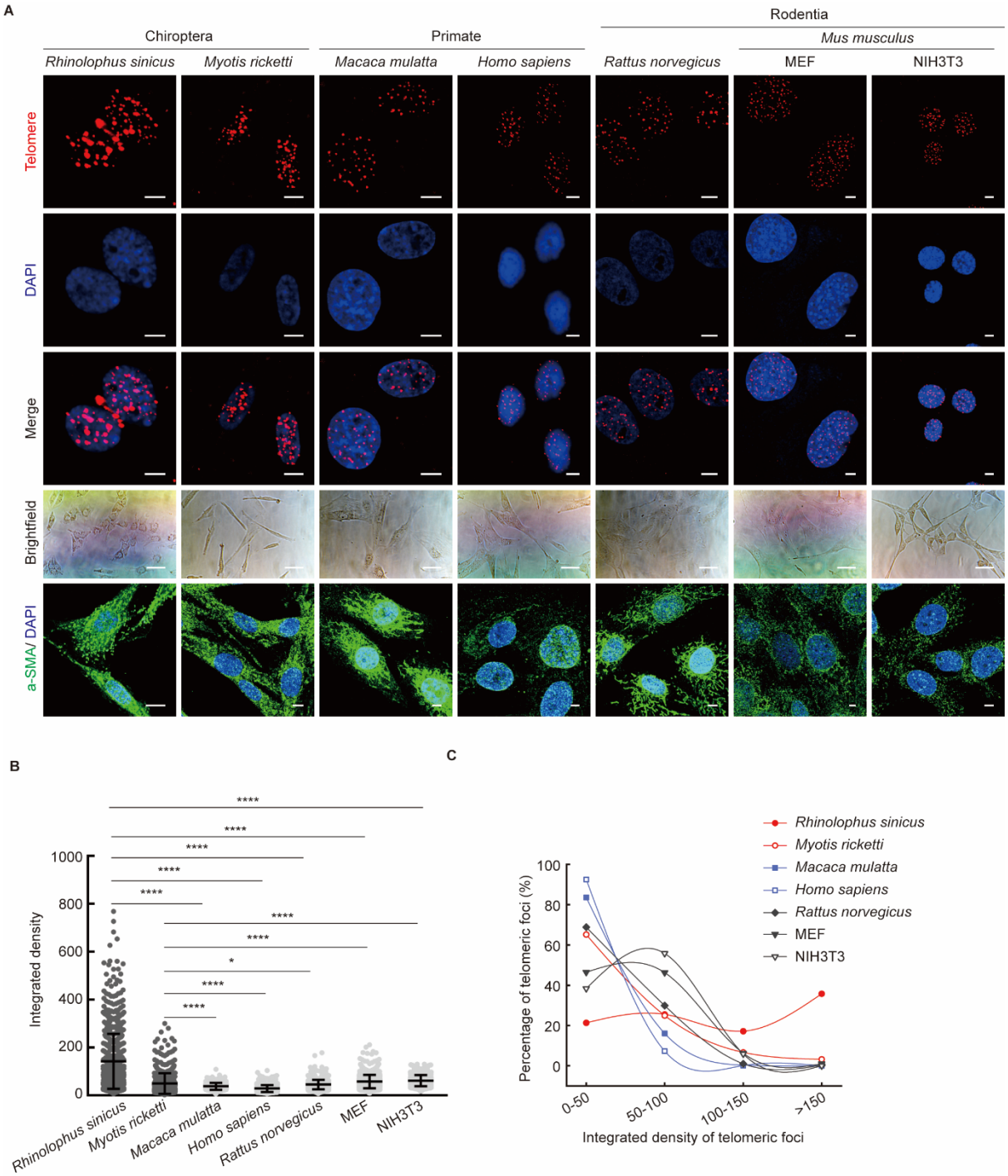

Supplementary Figure S1 Telomere fluorescence *in-situ* hybridization (T-FISH) of fibroblasts from multiple species

A: Representative T-FISH and cellular morphological images of fibroblast lines. Telomere probe (red) and DAPI (blue) were used for labeling. Antibody targeting α-SMA was used as a fibroblast marker. B: Quantification of telomeric T-FISH spots of each fibroblast line. Spots from 20 nuclei of each line were calculated. C: Integrated density distribution of T-FISH spots. Data represent mean±SD. *n*=3 biologically independent experiments unless otherwise stated. Scale bar=5 μm in T-FISH and α-SMA immunofluorescence staining, Scale bar=50 μm in cellular morphological images (Brightfield). MEF: Mouse embryos fibroblasts. *P*-values were calculated using a two-

tailed *t*-test. ns: Not significant; *: $P<0.05$; **: $P<0.01$; ***: $P<0.001$; ****: $P<0.0001$.

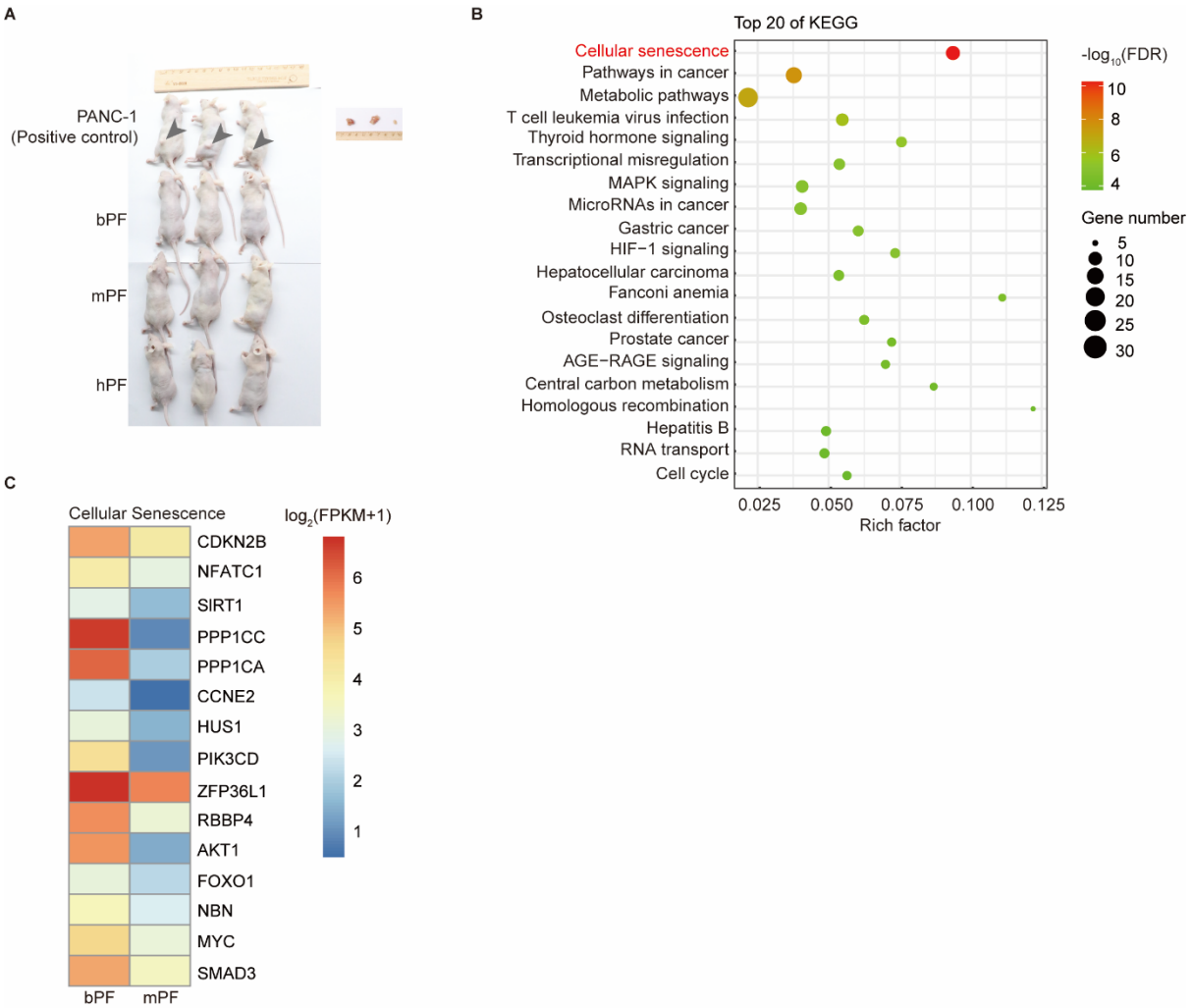

Supplementary Figure S2 Functional enrichment of highly expressed genes in bPF cells

A: Tumor formation evaluation in bPF, mPF, and hPF cells. Pancreatic cancer cell line PNAC-1 was used as an operational control. B: Kyoto Encyclopedia of Genes and Genomes (KEGG) analysis of highly expressed genes in bPF cells compared with mPF cells (FPKM fold-change>2). Pathways were ranked based on false discovery rate (FDR). C: Heatmap of enriched cellular senescence genes in bPF and mPF cells.

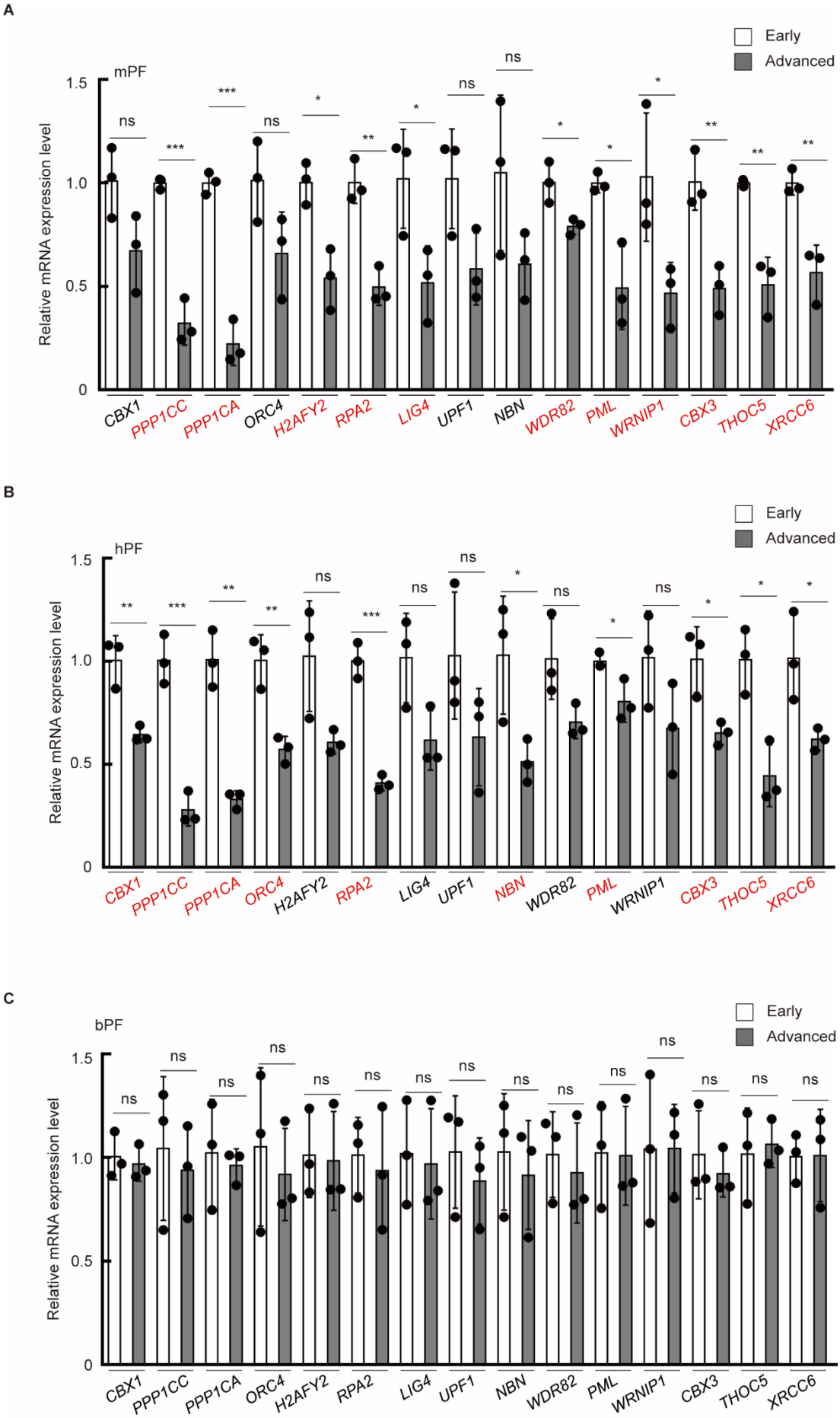
A
mPF
Early
Advanced
Relative mRNA expression level
1.5
1.0
0.5
0
ns
***
***
ns
*
**
*
ns
ns
*
*
*
**
**
**
CBX1
PPP1CC
PPP1CA
ORC4
H2AFY2
RPA2
LIG4
UPF1
NBN
WDR82
PML
WRNIP1
CBX3
THOC5
XRCC6
B
hPF
Early
Advanced
Relative mRNA expression level
1.5
1.0
0.5
0
**
***
**
**
ns
***
ns
ns
*
ns
*
ns
*
*
*
CBX1
PPP1CC
PPP1CA
ORC4
H2AFY2
RPA2
LIG4
UPF1
NBN
WDR82
PML
WRNIP1
CBX3
THOC5
XRCC6
C
bPF
Early
Advanced
Relative mRNA expression level
1.5
1.0
0.5
0
ns
ns
ns
ns
ns
ns
ns
ns
ns
ns
ns
ns
ns
ns
ns
ns
ns
CBX1
PPP1CC
PPP1CA
ORC4
H2AFY2
RPA2
LIG4
UPF1
NBN
WDR82
PML
WRNIP1
CBX3
THOC5
XRCC6

Supplementary Figure S3 qRT-PCR analysis of telomeric pathway genes

A-C: qRT-PCR detection of telomeric pathway genes at early and advanced passages in mPF (A), hPF (B), and bPF (C) cells. Data represent mean±SD. *n*=3 biologically independent experiments. *P*-values were calculated using two-tailed *t*-test. ns: Not significant; *: *P*<0.05; **: *P*<0.01; ***: *P*<0.001; ****: *P*<0.0001.

A

Gene	Ensembl ID	FPKM in bPF	FPKM in mPF	Fold change	*P* value	TelNet score
EPAS1	ENSG00000116016	122.02	0.81	150.03	2.92E -05	6
HNRNPK	ENSG00000165119	105.46	3.10	34.02	5.38E -03	7
SUMO2	ENSG00000188612	69.12	0.43	160.74	1.15E -02	6
CBX3	ENSG00000122565	39.63	1.19	33.39	2.89E -05	6
NR2F1	ENSG00000175745	25.48	0.66	38.60	6.29E -04	5
XRCC6	ENSG00000196419	16.61	0.80	20.85	9.73E -09	8

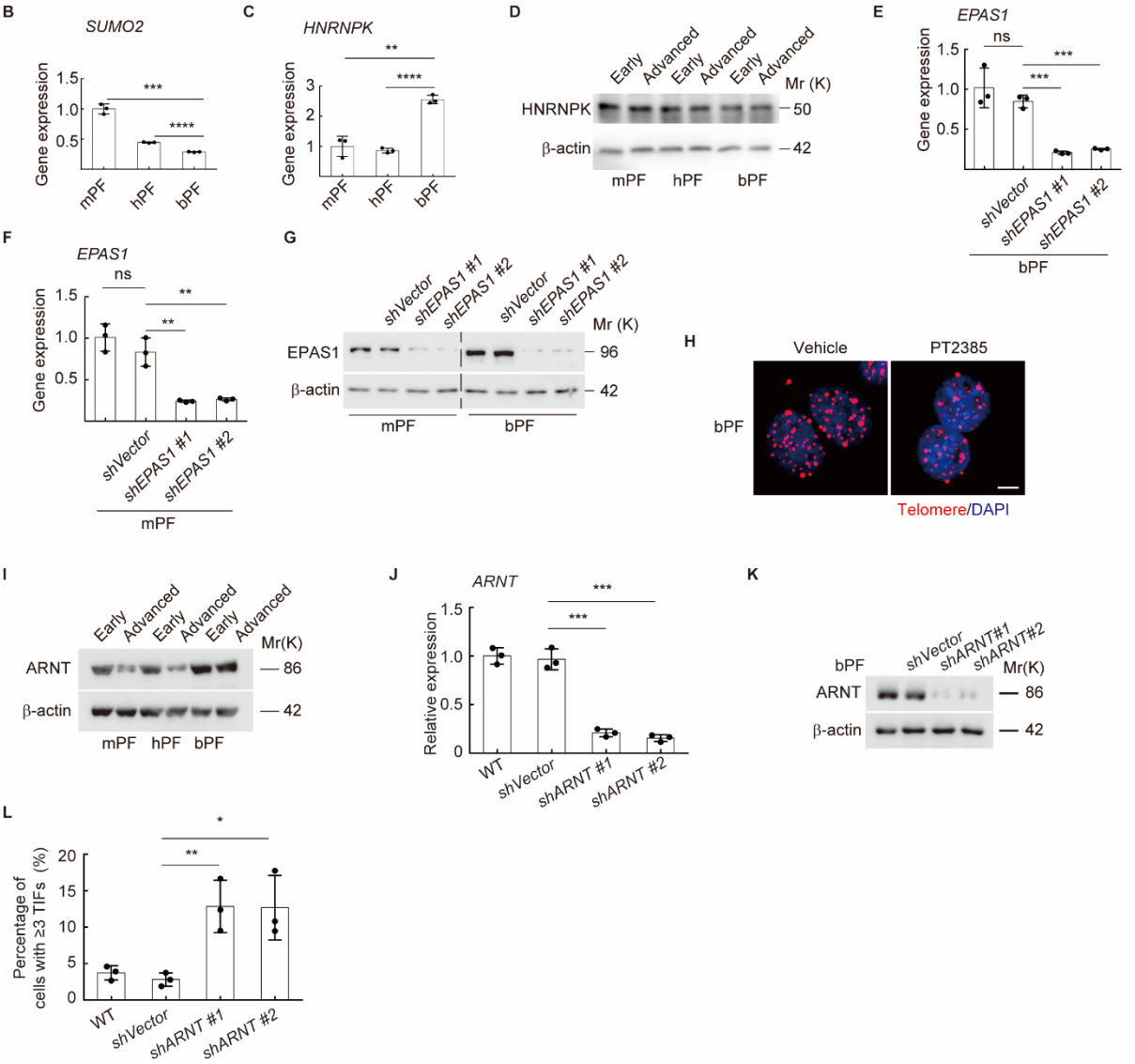

Supplementary Figure S4 Expression validation of telomere-related genes

A: List of highly expressed telomere-related genes in bPF cells (related to Figure 3A).

B: Transcriptional comparison of *SUMO2* in bPF, mPF, and hPF cells based on qRT-PCR. C: Transcriptional comparison of *HNRNPK* in bPF, mPF, and hPF cells based on qRT-PCR. D: Immunoblotting of HNRNPK in bPF, mPF, and hPF cells at early and advanced passages, respectively. β-actin was used as a loading control. E: Transcriptional validation of *EPAS1* knockdown in bPF cells. F: Transcriptional validation of EPAS1 knockdown in mPF cells. G: Immunoblotting validation of *EPAS1* knockdown in mPF (left) and bPF (right) cells. β-actin was used as a loading control. H: T-FISH of bPF cells with vehicle or 10 μmol/L PT2385 treatment for 7 d. I: Immunoblotting of ARNT in bPF, mPF, and hPF cells at early and advanced passages, respectively. β-actin was used as a loading control. J, K: qRT-PCR (J) and immunoblotting (K) validation of *ARNT* knockdown in bPF cells. β-actin was used as a loading control. L: Quantification of cells with ≥3 TIFs in bPF with or without *ARNT* knockdown. In total, 100 cells were analyzed for each sample. n=3 independent experiments unless otherwise stated. Scale bar=5 μm. Data represent mean±SD. P-values were calculated using a two-tailed student's t-test. ns: Not significant; *: P<0.05; **: P<0.01; ***: P<0.001; ****: P<0.0001.

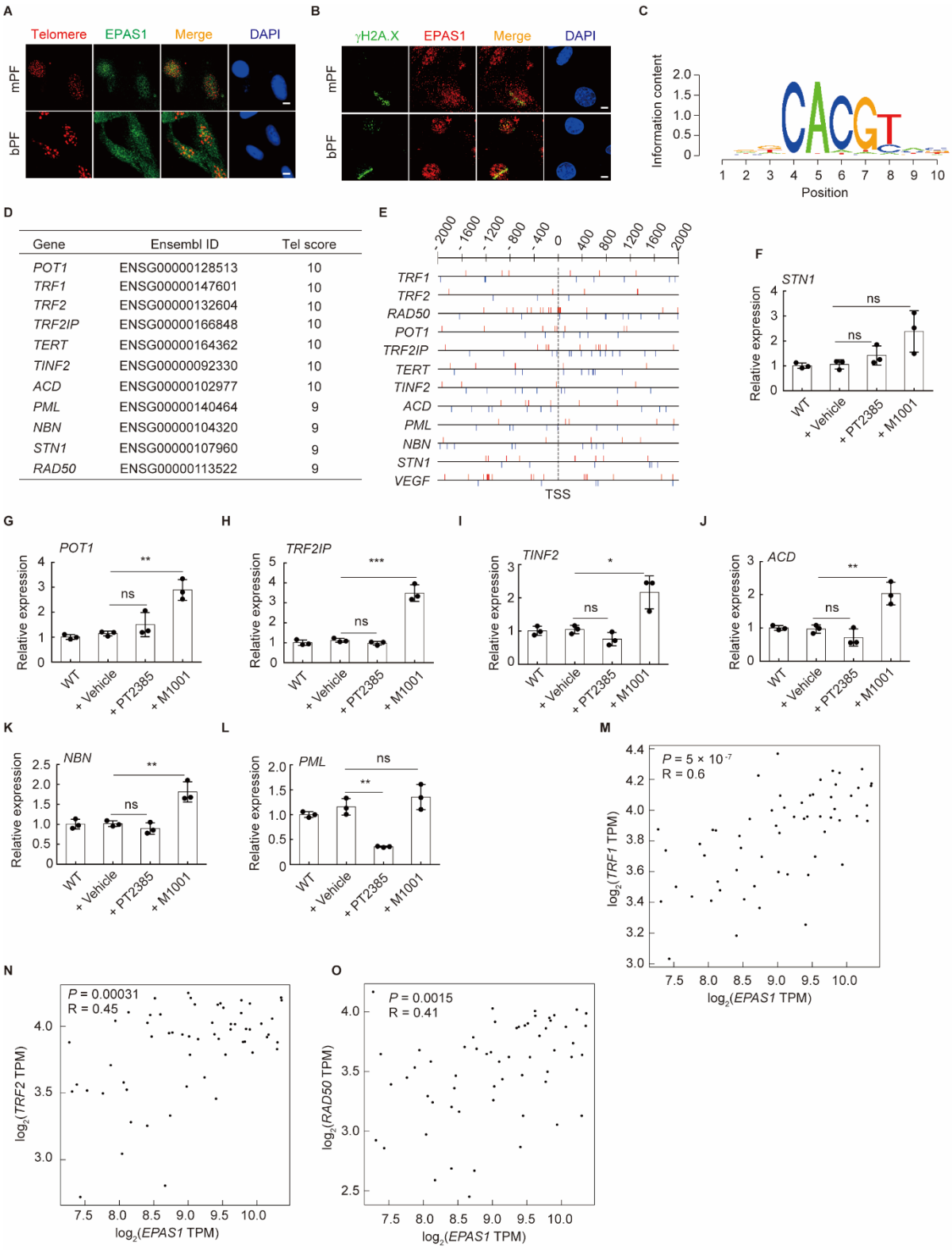

Supplementary Figure S5 Expression of telomere-related genes in response to PT2385 or M1001 treatment

A: Co-immunostaining of EPAS1 and telomeres in mPF and bPF cells using T-FISH combined with EPAS1 immunofluorescence. B: Co-immunostaining of EPAS1 and DNA damage marker γH2A.X in mPF and bPF cells. A UV laser was used to induce DNA damage. C: Predicted binding motif of EPAS1 obtained from online database

(http://cistrome.org/db/#/). D: List of telomere-related genes with score >9 in TelNet database. E: Distribution of EPAS1-binding motif in promoter regions of telomere-related genes (D). *VEGF* was included as a positive control. Red bars indicate binding sites on sense strand, blue bars indicate sites on antisense strand. F-L: qRT-PCR-based transcriptional analysis of *STN1* (F), *POT1* (G), *TRF2IP* (H), *TINF2* (I), *ACD* (J), *NBN* (K), and *PML* (L) in mPF cells under vehicle, 10 μmol/L PT2385, or 10 μmol/L M1001 treatment for 2 d. M, N, O: Pearson correlation analysis of *EPAS1* and *TRF1* (M), *EPAS1* and *TRF2* (N), and *EPAS1* and *RAD50* (O) in normal human lung tissues. Analysis was performed using GEPIA2 database (http://gepia2.cancer-pku.cn/#index). Scale bar=5 μm. n=3 independent experiments unless otherwise stated. Data represent mean±SD. P-values were calculated using a two-tailed student's t-test. ns: Not significant; *: P<0.05; **: P<0.01; ***: P<0.001; ****: P<0.0001.

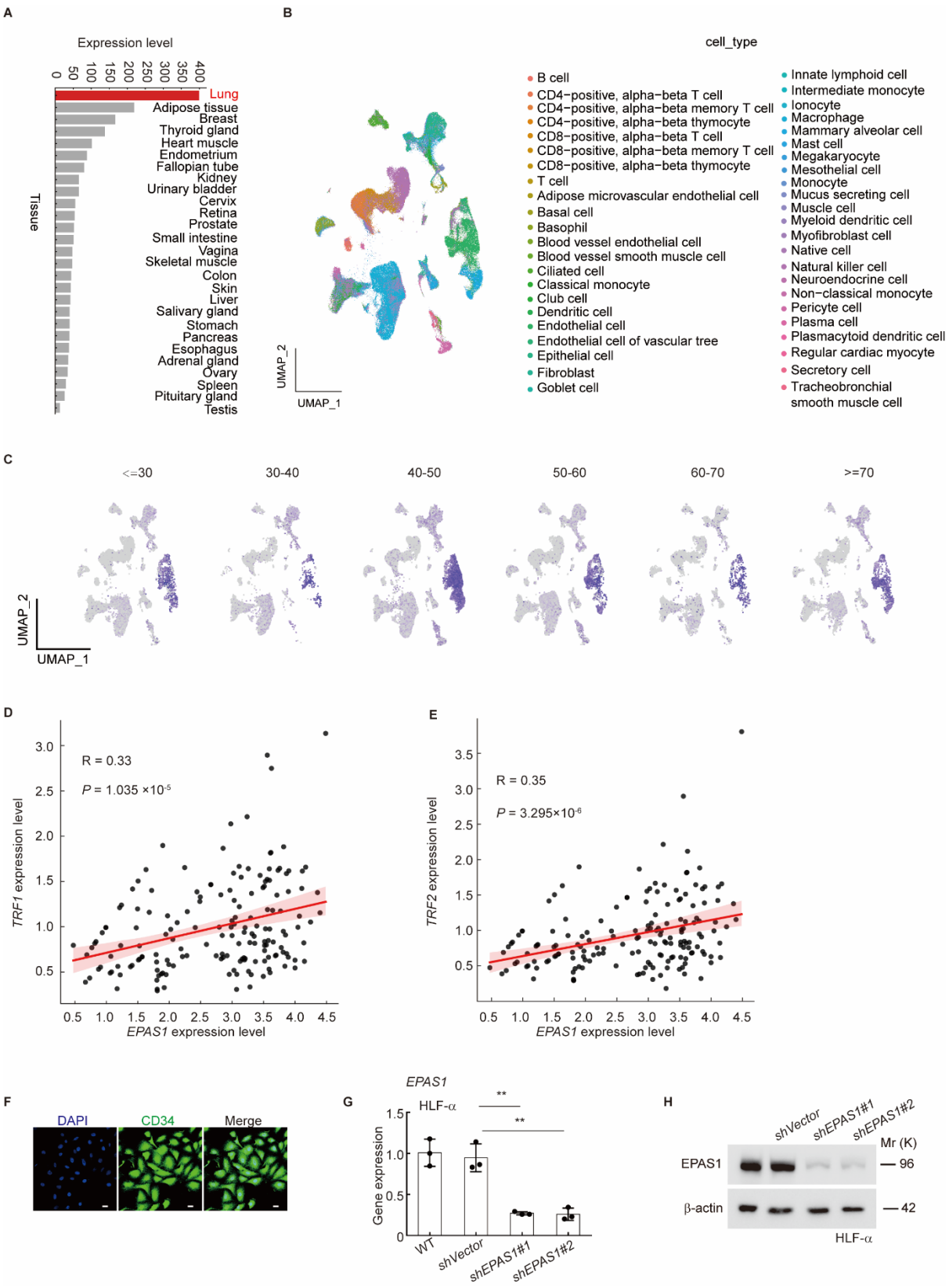

Supplementary Figure S6 High expression of EPAS1 in human pulmonary endothelial cells

A: Expression of *EPAS1* in major human organs and tissues. B: Uniform manifold approximation and projection (UMAP) visualization of all clusters colored by all cell

types. C: UMAP visualization of *EPAS1* expression dynamics in human pulmonary endothelial cells in various age groups. D, E: Pearson correlation analysis of EPAS1 and TRF1 (D), and EPAS1 and TRF2 (E) in single-cell transcriptome database of human pulmonary endothelial cells. Corresponding to Figure 5A to 5C. F: Immunostaining of endothelial cell marker of CD34 in *in vitro*-cultured HLF-α cells. G, H: qRT-PCR (G) and immunoblotting (H) validation of *EPAS1* knockdown in HLF-α cells. β-actin was used as a loading control. Scale bar=20 μm. n=3 independent experiments unless otherwise stated. Data represent mean±SD. P-values were calculated using a two-tailed student's t-test. ns: Not significant; *: P<0.05; **: P<0.01; ***: P<0.001; ****: P<0.0001.

Supplementary Figure S7

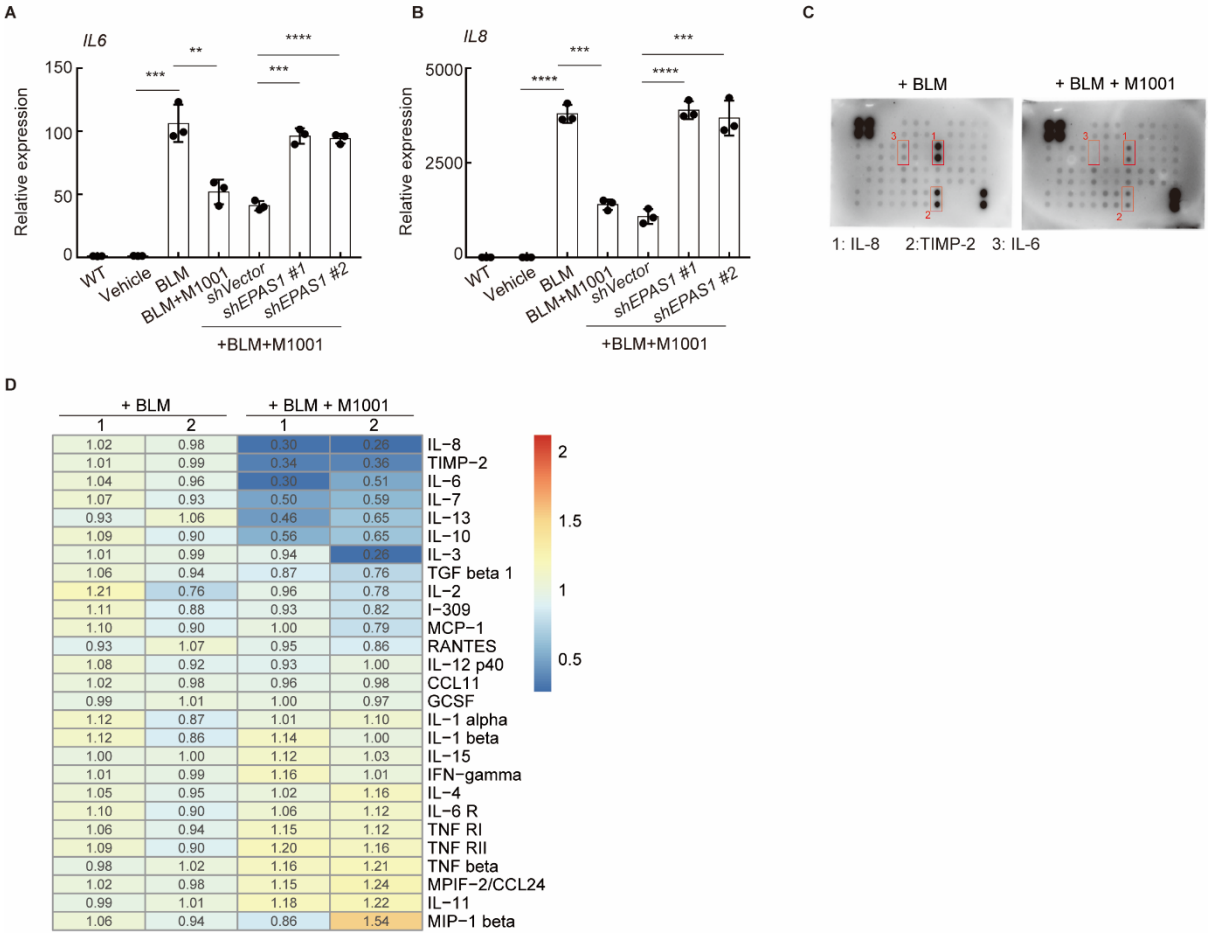

Supplementary Figure S7 qRT-PCR analysis of SASP factors in HLF-α cells under indicated treatments

A: qRT-PCR analysis of *IL6*. B: qRT-PCR analysis of *IL8*. C, D: Microarray blotting (C) and quantification (D) of SASP expression HLF-α cells with or without *EPAS1* knockdown. Cells were pretreated with vehicle or 200 μmol/L BLM for 16 h, followed by culture with 10 μmol/L M1001 for 7 d. n=3 independent experiments unless otherwise stated. Data represent mean±SD. P-values were calculated using a two-tailed student's t-test. ns: Not significant; *: P<0.05; **: P<0.01; ***: P<0.001; ****: P<0.0001.